JGR Earth Surface

RESEARCH ARTICLE

Key Points:

- We conducted physical model tests and numerical simulations to study particle sorting in scree slopes from a micromechanical perspective
- Relative particle size and shape factors are proposed to interpret the sorting feature described by a novel segregation index
- The dissipation rate of kinetic energy is a vital index relating to the particle migration distance, which determines the sorting feature

Correspondence to:

B.-B. Dai,
daibb@mail.sysu.edu.cn

Author Contributions:

Conceptualization: Bei-Bing Dai
Data curation: Fan-Yu Wu
Formal analysis: Bei-Bing Dai, Fan-Yu Wu, Yi-Hao Shi
Funding acquisition: Bei-Bing Dai
Investigation: Fan-Yu Wu, Wei-Tao Zhong, Yi-Hao Shi, Jin-Tao Qin
Methodology: Bei-Bing Dai
Project Administration: Bei-Bing Dai
Resources: Bei-Bing Dai
Software: Fan-Yu Wu, Yi-Hao Shi, Jia-Jun Yang
Supervision: Bei-Bing Dai
Validation: Wei-Tao Zhong, Jin-Tao Qin
Visualization: Wei-Tao Zhong
Writing – original draft: Fan-Yu Wu, Wei-Tao Zhong, Yi-Hao Shi, Jin-Tao Qin
Writing – review & editing: Bei-Bing Dai, Jun Yang

Particle Sorting in Scree Slopes: Characterization and Interpretation From the Micromechanical Perspective

Bei-Bing Dai[1,2] , **Fan-Yu Wu[1]** , **Wei-Tao Zhong[1]** , **Yi-Hao Shi[1]** , **Jin-Tao Qin[1]** , **Jia-Jun Yang[1]** , **and Jun Yang[3]**

[1]School of Civil Engineering, Sun Yat-sen University, Guangzhou, China, [2]Southern Marine Science and Engineering Guangdong Laboratory (Zhuhai), Zhuhai, China, [3]Department of Civil Engineering, The University of Hong Kong, Hong Kong, China

Abstract Particle sorting is one of the most interesting phenomena observed in the formation of scree slopes. We present a study of this phenomenon through physical model tests and numerical simulations at the grain scale, with a focus on the link between the degree of sorting and particle attributes, as well as the underlying mechanisms. By characterizing the degree of sorting with the graphic segregation index, we show that the degree of sorting increases as the difference in particle size and shape between the component materials of the deposited mixture increases. We propose two factors, the relative size factor (SF_r) and relative shape factor (OR_r), and show that the degree of sorting increases with the absolute values of these two factors ($|SF_r|$ and $|OR_r|$). By monitoring the motions of tracer particles in the numerical simulations, we found that particle migration proceeds in a periodical mode of "collision/friction ⇌ regaining ⇌ collision/friction." Also, we performed energy analyses, revealing that relatively large and rounded particles tend to have a lower rate of kinetic energy dissipation, migrate at a higher velocity over a longer period of time, and have a larger migration distance. In addition, we define a relative kinetic energy dissipation rate $|D_{k\_r}|$ and find that it is positively correlated with $|SF_r|$ and $|OR_r|$; the discrepancy in particle size and shape between the component materials is responsible for the difference in their kinetic energy dissipation rates, and it is the latter that determines their migration distance difference and sorting features.

Plain Language Summary A scree slope is an inclined accumulation of the rock fragments and sand grains sourced from a weathered and failed cliff. Particle sorting is an interesting phenomenon observed in scree slopes, which refers to the special arrangement of particles in terms of particle size and shape along the longitudinal direction of slopes, and affects the overall motion of granular mass flows during the formation and failure of scree slopes. Through physical model tests and numerical simulations at a particulate scale, we attempt to understand the sorting phenomenon at a fundamental level. We found that the degree of sorting in a scree slope increases with the increasing discrepancy in particle size and shape between the component materials. We identified a positive correlation between the sorting index and the relative particle size and shape factors. We reveal that the difference in particle size and shape is associated with the difference in the dissipation rate of kinetic energy of particles, and the latter determines the difference in the migration distance of particles and the sorting feature. Understanding the sorting phenomenon is important for the evaluation of the influence of geophysical mass flows in scree slopes and for the prevention of related hazards.

1. Introduction

A scree (talus) slope is characterized by an inclined accumulation of rock debris sourced from the upper part of a weathered cliff at the foot of the cliff. Scree slopes are widely encountered in high, frigid mountainous regions and have some interesting geomorphic features (Caine, 1969; Kirkby & Statham, 1975; Sass, 2006). The formation of scree slopes, as shown in Figure 1, is a complex process that involves the detachment, descent, movement, and accumulation of weathered and failed rock. The mechanics of this dynamic process have been of long-standing interest in a number of fields (e.g., Bertran et al., 1997; Bithell et al., 2014; Caine, 1969; De Blasio & Sæter, 2009, 2015; Jomelli & Francou, 2000; Kirkby & Statham, 1975; Obanawa & Matsukura, 2006; Sass, 2006, 2007; Savage & Lun, 1988; Sheng et al., 2021; Utili & Crosta, 2011a).

The movement and accumulation of debris masses during the formation of scree slopes is a type of geophysical mass flow (Gray & Thornton, 2005; van der Vaart et al., 2018). These slope deposits are primarily composed of
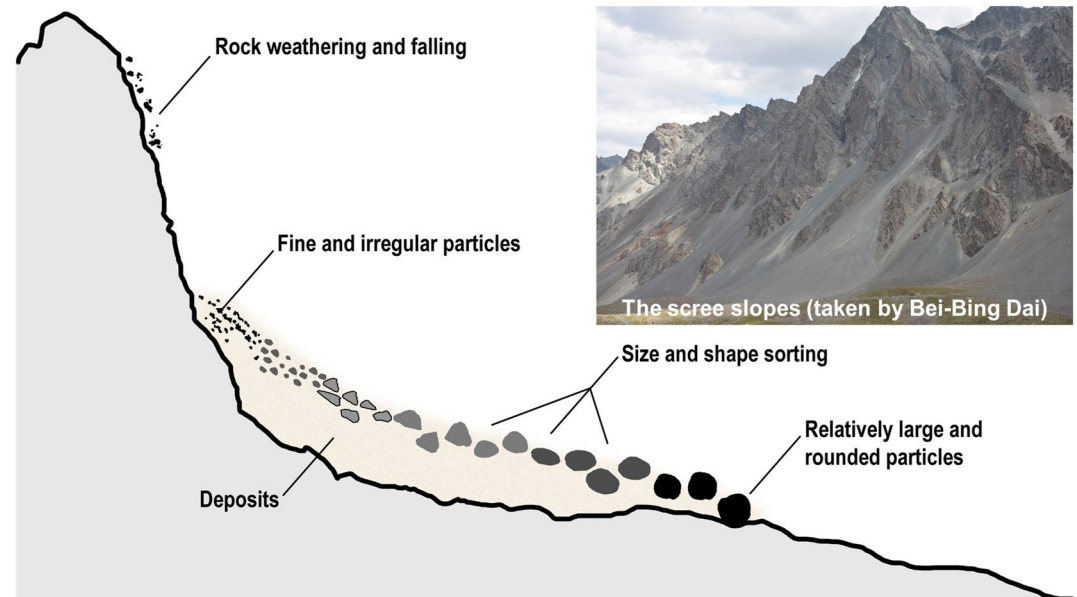
Figure 1. Schematic description of scree slope formation with an inset showing the scree slopes in Tianshan.

rock fragments and sand grains with weak or no interparticle bonding, and they typically have a loose structure (Pei, 2016; Zhang et al., 2010). Thus, scree slopes tend to deform and fail in response to relatively small external disturbances (Carson, 1977; Pei, 2016). Such scree slope failures are different from the deep-seated slope failures observed in soil mechanics (Martin, 2000; Utili & Crosta, 2011a). Geophysical mass flows induced by scree slope failures can be described as shallow granular free-surface flows or shallow granular avalanches (Gray & Chugunov, 2006; Gray & Thornton, 2005), and they are, to some extent, analogous to debris flows, snow avalanches and pyroclastic flows (Gray & Kokelaar, 2010; Johnson et al., 2012; van der Vaart et al., 2018). Of primary interest is the particle sorting (i.e., segregation) phenomenon observed in scree slopes. A large number of field investigations have indicated that the arrangement of particles in scree slope deposits has obvious sorting features (e.g., Bertran et al., 1997; De Blasio & Sæter, 2009, 2015; Evans & Hungr, 1993; Gardner, 1970; Jomelli & Francou, 2000; Kotarba & Strömquist, 1984; McGrath et al., 2013; McSaveney, 1971; Pei, 2016; Pérez, 1989; Statham, 1976; Zhang et al., 2010): from the upper part to the lower part of a scree slope, the size and roundness of the particles tends to increase; that is, relatively large and rounded particles are located around the base of the slope, and relatively small and irregular particles are present near the crest of the slope (see Figure 1).

The phenomenon that particles of dissimilar properties segregate is widely present in geophysical mass flows such as landslides and snow avalanches (Gray & Kokelaar, 2010; De Hass et al., 2015; Zhou et al., 2020) and in granular flows associated with industrial processes such as mining and bulk solids conveying (Saxton et al., 2008; Dai et al., 2021). Coarse particles tend to preferentially migrate towards the flow front, leading to a specific structure in the flow deposits: coarse particle domination at the front of the deposit and small particle domination at the rear (Gray & Kokelaar, 2010; Zhou et al., 2020) (Figure 1). This particle-sorting induced structure can in turn exert a strong impact on the bulk motion of the geophysical mass flows, including local rheology, flow mobility and run-out distance (Bi et al., 2016; Gray & Chugunov, 2006; Gray & Kokelaar, 2010; Phillips et al., 2006; van der Vaart et al., 2018). Therefore, it is critical to gain a deep understanding of the phenomenon of particle sorting to evaluate the potential influence of geophysical mass flows occurring during the formation and failure of scree slopes, and to take corresponding countermeasures for the mitigation of scree-slope related hazards.

Kirkby and Statham (1975) and Statham (1976) established a mathematical model based on an essential parameter—the dynamic angle of friction. This parameter was used to characterize the overall friction effect of a particle moving on a slope surface. They attributed the occurrence of particle size sorting to the difference in dynamic angles of friction between coarse and fine particles. Following Kirkby and Statham (1975), Gabet (2003), Gabet and Mendoza (2012), and DiBiase et al. (2017) proposed a particle-based ravel transport model to account for the effects of grain size and surface roughness on the spatial pattern of steep hillslope sediment transport. De Blasio

and Sæter (2009, 2015) performed small-scale physical model tests to mimic the formation and evolution of scree slopes, and probed the underlying mechanism by examining the dynamics of falling grains on an inclined granular bed. They assumed that the longitudinal size sorting along the slope may be attributed to the difference in the modes of energy loss of particles impacting the granular bed: large particles tend to lose most energy upon the first impact at the falling point and then either stop or migrate towards the distal part of the slope bed, while small particles undergo several bouncing motions, losing energy and being deposited near the initial point of impact.

Interestingly, the field surveys and measurements performed by several researchers have suggested that the particle arrangements in some scree slopes do not exhibit a distinct sorting feature (Caine, 1967, 1969; De Blasio & Sæter, 2010; Gardner, 1968; Haas et al., 2012; Luckman, 1971; Pérez, 1985; Thornes, 1971). Other researchers have shown that the sorting feature can be gradually erased during the evolution of a scree slope (Bones, 1973; De Scally & Owens, 2005; Gardner, 1968; Jomelli & Francou, 2000). De Blasio and Sæter (2010) observed during a field survey in Drammen (Norway) that the slope deposits do not display a marked longitudinal variation in block size but rather a sorting feature in block shape. Specifically, regular blocks with relatively high aspect ratios are more likely to travel along the slope and arrive at the toe. Thus, it is evident that particle sorting in scree slopes is an interesting but challenging problem that is not yet fully understood in terms of both the characterization and interpretation of the underpinning mechanisms.

Recently, discrete element method (DEM) simulations have been used to investigate the formation and evolution of scree slopes. Utili and Crosta (2011b) performed a two-dimensional (2D) DEM simulation to model cliff retreat, but their studies did not concentrate on the dynamics involved in the formation and evolution processes nor the basic characteristics (e.g., particle sorting) of scree slope deposits. Bithell et al. (2014) reported a 2D DEM study on the development of scree slopes, in which all debris masses to be accumulated were generated once and then released together to form a scree slope; the true dynamic process responsible for the formation of scree slopes was not accounted for. Zhou and Ng (2010) used a similar approach to perform DEM simulations of debris flows and examine reverse segregation. Again, current numerical studies basically fail to reveal the underlying mechanism of particle sorting from a fundamental perspective by capturing the true formation and evolution processes. These approaches have also not provided a quantitative analysis of particle sorting features by considering the effect of basic particle attributes.

To address this limited understanding, we present a study that aims to elucidate the phenomena of particle sorting observed in scree slopes at a micromechanical level. Using granular materials with various particle sizes and shapes, we performed a series of model experiments of scree slopes and quantitatively characterized the effects of particle attributes on the sorting feature. We then performed three-dimensional (3D) DEM simulations to mimic the formation of scree slopes and to further examine the mechanisms for the sorting feature. In the numerical simulations, we monitored particle movements, particle interactions and energy variations to trace the dynamics of the debris mass at a particulate scale and to probe the influence of basic particle attributes on the particle motions and energy dissipation. The findings from this study contribute to a deeper understanding of the sorting phenomena in scree slope deposits and the behavior of geophysical mass flows in scree slopes.

2. Experimental and Numerical Implementation

2.1. Experimental Device and Materials

The experimental device, as shown in Figure 2a, is made up of a welded steel frame. The dimensions are 3.6 m in length, 0.6 m in width, and 1.8 m in height. At the top of the steel frame is a V-shaped hopper for releasing particles. The steel plate modeling the bed rock can be divided into three sections: the kinetic migration section, accumulation section and buffer section. The angles of the kinetic migration and accumulation parts relative to the horizontal plane are set to 44° and 11°, respectively. Along the two long edges of the steel plates stand the two vertical transparent acrylic plates (0.6 m in height) to prevent particles from moving outside and for ease of observation. A black grid with the horizontal and vertical spacings being both 2 cm, was drawn on the transparent plates to permit comparison of the accumulation characteristics of different granular masses (see Figure 2a).

The basic particle attributes play a critical role in the mechanical behavior of granular materials (Cavarretta et al., 2010; Yang & Wei, 2012; Dai et al., 2016; Dai, 2018a) (Table 1). We used five granular materials (i.e., glass bead, dolomite rock grain, cobble, sandstone, and basalt rock grain) to study the effect of particle size and shape on the characteristics of accumulated granular mass (see Figures 2b–2f). The particle shapes for these materials
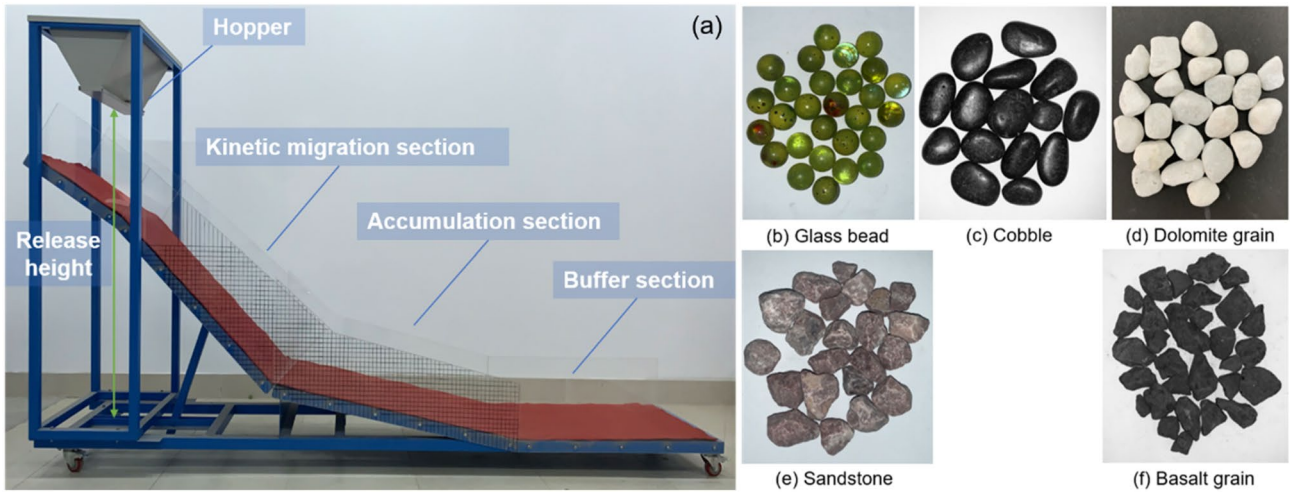
Figure 2. Side view of the experimental device and the testing materials.

vary from round to angular, and there are three particle size levels. The effect of interparticle friction and particle mineralogy is beyond the scope of this study and is partly isolated by performing experiments in which material type is not varied in a certain test series. The particle densities of the materials used do not differ considerably (Table 1); thus, the particle mass effect is, to some extent, equivalent to the particle size effect. In the experiments, the transparent glass beads are dyed yellow for ease of being distinguished from other materials. In addition, we laid a thin blanket on the steel plate to increase the bed roughness. We have also referred to the literature (e.g., De Blasio & Sæter, 2015) for the test equipment design and material use. We used a shape factor called the overall regularity (OR) to characterize the particle shape, which is expressed as (Yang & Luo, 2015):

$$OR = \frac{AR + R + C}{3} \tag{1}$$

where the roundness (R), aspect ratio (AR) and convexity (C) are introduced in detail in Appendix A. The effect of climate-dependent slope surface friction conditions is not considered in the proposed test program.

2.2. Experimental Procedure

To undertake a systematic study on the effect of particle size and shape, we selected one material as the base material and then added another material of equivalent mass into the base material to create a mixture for testing. The mixture scheme is shown in Table 2, and the individual letters a, b and c in Table 2 are the codes that represent the three size levels. The weight of each mixture is 80 kg, with the base and addition materials having an equal weight, and a small portion (5 kg) of mixtures are used for each release. Thus, we performed the release of each mixture 16 times to complete the testing of a mixture with a mass of 80 kg. The release height was 1.5 m. After the release of all mixture masses, we divided the accumulated mass into several sections at an equal

Table 1
Basic Attributes of the Testing Materials

| Particle type	Density (g/cm³)	Minerals	Roundness (R)	Aspect ratio (AR)	Convexity (C)	Overall regularity (OR)	Particle size (mm)
Glass bead	2.62	Quartz	1.000	1.000	1.000	1.000	12, 16, 25
Cobble	2.90	Quartz	0.936	0.731	0.664	0.777	20~30
Dolomite grain	2.94	Calcium/Magnesium carbonate	0.802	0.841	0.650	0.764	9~12, 10~20, 20~30
Sandstone	2.68	Quartz	0.872	0.737	0.629	0.746	10~20, 20~30
Basalt grain	2.76	Quartz	0.863	0.721	0.610	0.731	6~9, 10~20, 20~30

Table 2
Experimental Mixture Scheme

Test series	Base material	Particle size of base material (mm)	Added material	Particle size of added material (mm)		
				a	b	c
I	Basalt grain (B)	6~9	Glass bead (G)	12	16	25
			Dolomite grain (D)	10~20	20~30	30–50
			Sandstone (S)	\	\	20–30
II	Glass bead (G)	25	Dolomite grain (D)	6~9	10~20	20~30
			Sandstone (S)	\	10~20	\
			Basalt grain (B)	6~9	10~20	20~30
III	Cobble (C)	20~30	Dolomite grain (D)	6~9	10~20	20~30
IV	Dolomite grain (D)	30~50	Glass bead (G)	\	16	\
			Sandstone (S)	\	10~20	\
			Basalt grain (B)	6~9	10~20	\

horizontal interval of 10 cm, separated the added material from the base material for each section, and weighed the mass of the two constituent materials to determine their mass fractions in various sections of the deposits.

2.3. Numerical Model Setup

The DEM program particle flow code (PFC) has been shown to be a powerful numeric tool to investigate the mechanical behavior of granular materials (Dai et al., 2015, 2019, 2021; Gu et al., 2015, 2017; Li & Yu, 2010; Yang & Dai, 2011). We used PFC3D in this study to mimic the formation of scree slopes and micromechanically analyze the effect of particle attributes on the formation and characteristics of scree slopes. Figure 3 shows the numerical model setup, the dimensions of which are the same as those of the physical apparatus. We do not use
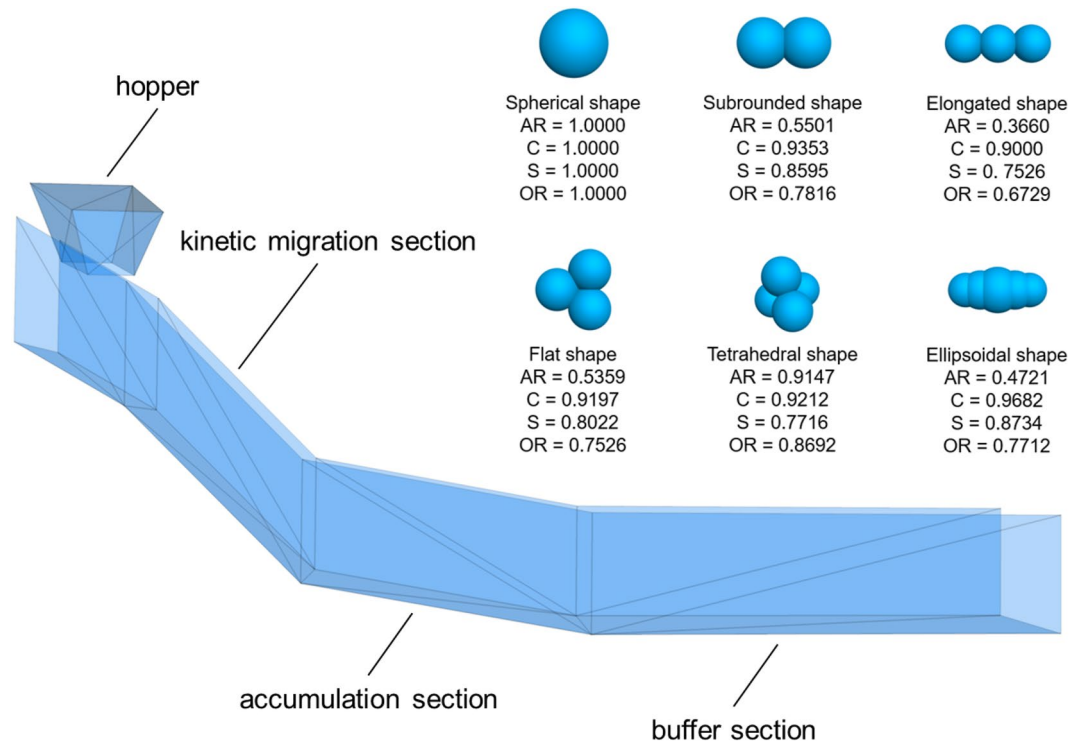
Figure 3. Numerical model and particle shapes considered in the simulation.

Table 3
DEM Modeling Parameters

Parameter	Value
Particle density, ρ (g/cm^3)	2.65
Particle diameter, d (mm)	15, 24, 32, 50
Interparticle friction, μ_s	0.5
Wall friction, μ_w	0.5
Normal stiffness of particles (walls), k_n (k_{wn}) (N/m)	10^5
Shear stiffness of particles (walls), k_s (k_{ws}) (N/m)	10^5
Local damping, α	0.05
Viscous damping, β	0.2

the periodic boundaries for lateral walls for consistency with the laboratory apparatus. The density of the numerical particle is 2.65 g/cm^3, and the particle size, which is characterized by the diameter of a spherical volume-equivalent particle, ranges from 15 to 50 mm. We used a linear elastic contact model to describe the contact behavior between particles. The particle stiffness in the normal and tangential directions is 10^5 N/m, and so is the wall stiffness. This stiffness value is comparable to the values for typical sand grains (Wang & Coop, 2016) and is thus considered to be reasonable. The interparticle and particle–wall friction coefficients are set to 0.5, and the local and viscous damping values are specified to be 0.05 and 0.2, respectively. The walls of the hopper have the same stiffness as the other walls. In the same manner as applied with respect to the real apparatus, the numerical model is divided into three sections, as shown in Figure 3. The model parameters are shown in Table 3. We have referred to many studies (e.g., Lu & Hsiau, 2008; Sitharam et al., 2002; Zhou & Ng, 2010; Zhou & Sun, 2013) to determine the values of numerical model parameters and ensured that the parameter values used can help capture the basic behavior of soil and rock materials in scree slope formation.

According to the rule of clump particles in PFC3D, we combined multiple spheres to generate particles of various shapes, which is a particle generation technique that has been used by many other researchers (Dai et al., 2017; Dai, 2018b; Li & Yu, 2010; Yang et al., 2013). We used six particle shapes (see Figure 3), including spherical, subrounded, elongated, flat, tetrahedral and ellipsoidal shapes, to approximately represent the diverse particle morphologies in the laboratory experiments. The comprehensive shape factor *OR* (i.e., overall regularity) was also used to characterize the shape of the modeled particles, with roundness *R* in Equation 1 replaced with sphericity *S*, which is the squared ratio of diameters between the volume-equivalent and surface-equivalent spherical particles (Pabst & Gregorova, 2007; Robinson & Friedman, 2002; Wadell, 1932, 1935). The values of the shape factors are listed in Figure 3.

Although the definitions of roundness and sphericity are not exactly the same, their values are positively correlated, as indicated by Zhou et al. (2018). The determination of particle roundness is based on 2D image analysis with a focus on 10 representative grains in this study (see Appendix B); thus, the roundness is considered to be an average value from 10 2D image analyses, which may, to some extent, help eliminate the difference between the 2D and 3D cases. Thus, we assume that the overall regularity factor can reasonably capture the basic shape characteristics in both experiments and numerical simulations and contribute to the consistent findings in this study, although the definitions of roundness and sphericity are not the same. In addition, the overall regularity factor (*OR*) cannot characterize multiscale shape features such as small-scale roughness (Nie et al., 2022).

2.4. Numerical Simulation Scheme

The execution of numerical simulations broadly follows the experimental procedure. For each run of the simulation, two types of clumped particles are uniformly mixed and contained in the modeled granular hopper. The mixture scheme is shown in Table 4. The weight of each component material is 4.8 kg, and a tracer particle

Table 4
Numerical Mixture Scheme

Simulation series	Base material	Particle size of base material (mm)	Added material	Particle size of added material (mm)		
				a	b	c
I	Tetrahedral shape (TS)	15	Spherical shape (SS)	24	32	50
			Subrounded shape (SR)	24	32	50
			Ellipsoidal shape (ES)	24	32	50
II	Spherical shape (SS)	50	Elongated shape (EG)	15	24	32
			Flat shape (FS)	15	24	32
			Tetrahedral shape (TS)	15	24	32
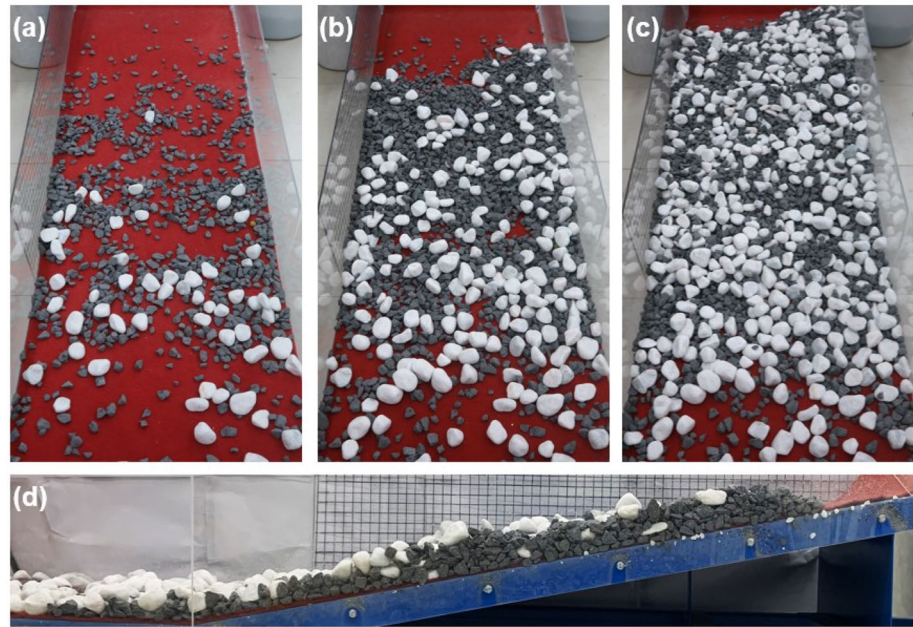
Figure 4. Evolution of the accumulated granular mass, with the states after (a) 2 times of release of mixture, (b) 6 times of release of mixture, (c) 16 times of release of mixture, and (d) the side view of deposits.

is set for close observation. When the baffle is removed, particles fall onto the artificial slope under gravity ($g = 9.8$ m/s^2). To determine whether the accumulated mass arrived at an equilibrium state, we introduce a cycling requirement that specifies an upper limit (1‰ in this study) for the ratio between the maximum unbalanced force magnitude and the average magnitude of forces acting upon the particle entities. If the ratio value is less than the upper limit (1‰), the accumulated mass is assumed to have reached a static state. Amid the simulations, we monitored various quantities, including particle motions and energies.

3. Experimental and Numerical Observations

3.1. Segregation Profiles

Figure 4 shows the typical accumulation process of a binary mixture composed of dolomite (in white) and basalt (in dark gray) aggregates for the test of IV-D-B(b). In this study, "D" refers to dolomite aggregates, and "B" stands for "basalt aggregates." Other abbreviations are given in Table 2. The particle sizes of the two aggregates are $d = 30\sim50$ mm and $d = 10\sim20$ mm for the dolomite and basalt aggregates, respectively. The front and side views of deposits indicate that relatively large and round particles (i.e., dolomite aggregates) tend to travel to the distal part of the board, and most basalt aggregates, which are relatively small in size and irregular in shape, do not migrate along the board as far as the dolomite aggregates and are mostly deposited in the upper part. Figure 4d also shows that the dolomite aggregates are primarily distributed at the top of deposits, creating a distinct stratification structure. That is, particle segregation occurs along the depth of accumulated deposits. However, stratification is beyond the scope of this study. We also did not observe a particle crushing phenomenon; thus, this phenomenon is assumed to play a minor role in the occurrence of particle sorting.

Figure 5 plots the variation in the concentration of small particles with the normalized horizontal distance, which is also called the segregation profile of accumulated mass. The profiles in Figure 5a are for the test series of I-B-G, in which the mixture comprises the base material of basalt aggregates ($d = 6\sim9$ mm) and the addition material of glass beads at three size levels (i.e., $d = 12$ mm, 16 mm, and 25 mm). There is a clear decreasing trend in the mass fraction of small particles, P, against the normalized horizontal distance, X/X_0, wherein X_0 is the horizontal spread distance of deposits from the tail to the front, indicating that relatively small and irregular basalt aggregates tend to be located at the upper part of the board, while large and rounded glass beads are prone to move further to the lower part. The segregation curve for I-B-G(a) is lower than that for I-B-G(c) in the upper part but
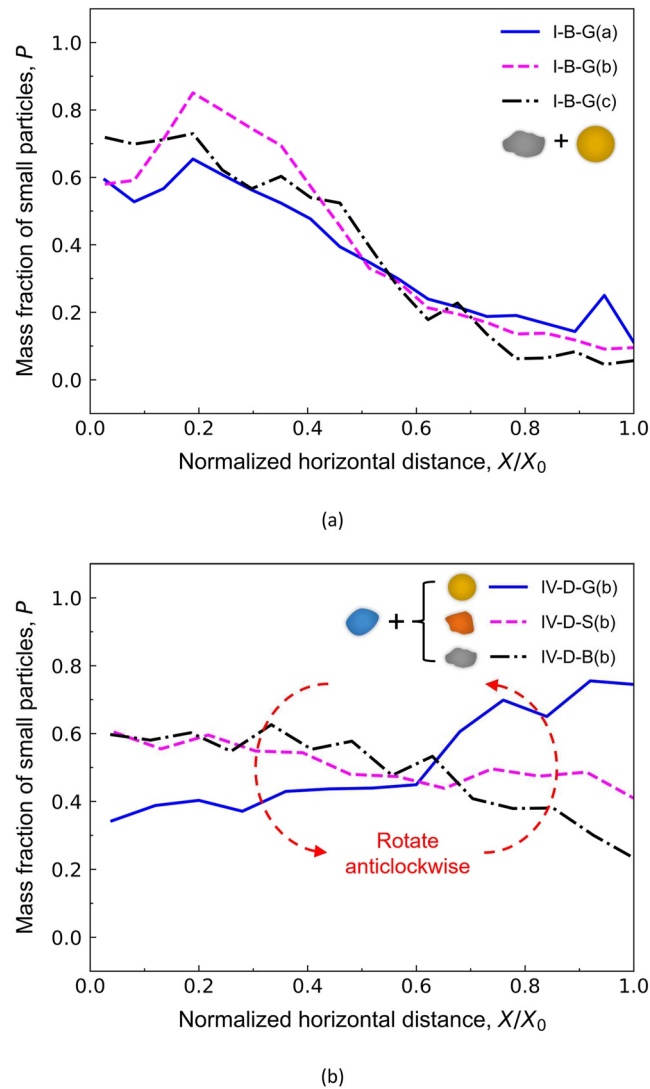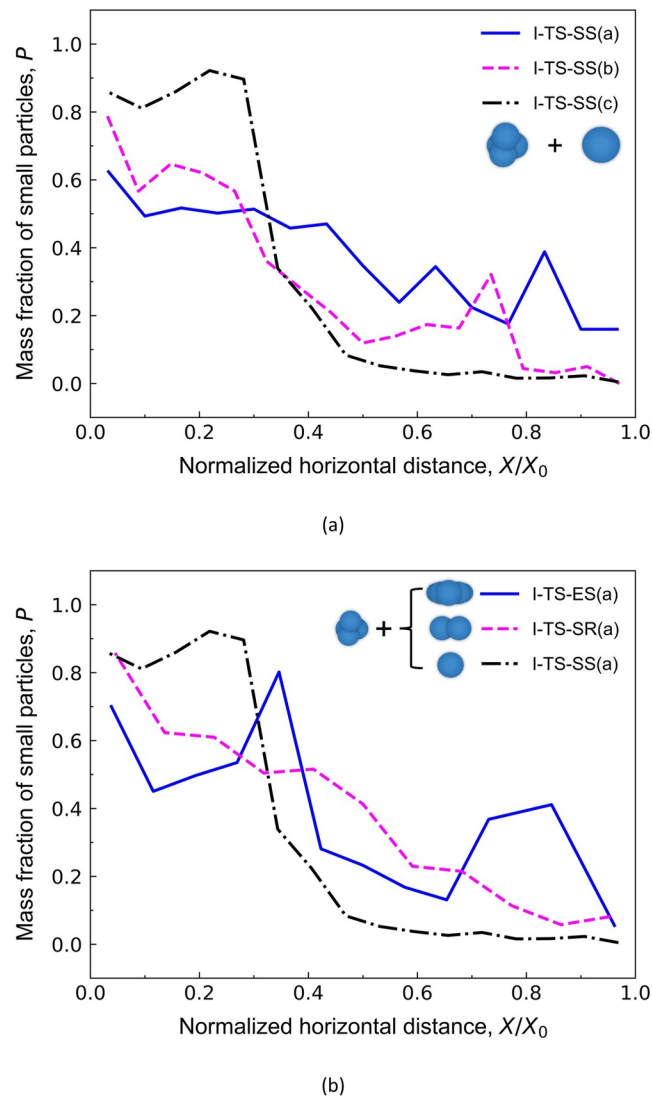
Figure 5. Segregation profile curves for (a) test series of I-B-G(a), I-B-G(b), and I-B-G(c), and (b) test series of IV-D-G(b), IV-D-S(b), and IV-D-B(b).

is higher than that in the lower part, with the curve for I-B-G(b) lying in between. Such observations signify a potential influence resulting from the particle size; increasing the size of glass beads makes more of them travel to the lower part of the board and leads to a more noteworthy segregation phenomenon.

Figure 5b shows the segregation profile curves for the IV-D-G(b), IV-D-S(b), and IV-D-B(b) tests, in which the base material is dolomite aggregates and the addition materials (i.e., glass beads, sandstone and basalt aggregates) have different particle shapes. The particle sizes of the addition materials are in the range of $d = 10 \sim 20$ mm, which is lower than that ($d = 30 \sim 50$ mm) for the base material. IV-D-S(b) and IV-D-B(b) show a normal segregation pattern; that is, large particles (base material) are primarily distributed in the lower part, and small particles (sandstone or basalt aggregate) are primarily distributed in the upper part. The mass fraction P for IV-D-S(b) is lower than or close to that for IV-D-B(b) in the upper part but is higher in the lower part. This is because the shape ($OR = 0.731$) of basalt aggregates, as indicated in Table 1, is more irregular than that ($OR = 0.746$) for sandstone grains, and it is typically more difficult for particles with more irregular shapes to migrate further towards the toe of slope deposits through either sliding or rolling behaviors. Thus, the mass fraction of basalt aggregates in the upper part is relatively large but is comparatively small in the lower part.

Figure 6. Segregation profile curves for (a) the simulation series of I-TS-SS(a), I-TS-SS(b), and I-TS-SS(c), and (b) the simulation series of I-TS-ES(a), I-TS-SR(a), and I-TS-SS(a).

Of particular interest is the observation in Figure 5b that the test of IV-D-G(b) shows a reverse segregation pattern; that is, small particles (glass beads) are primarily distributed in the distal part of the board, with most large particles (dolomite aggregates) being in the upper part. This phenomenon is primarily due to the effect of particle shape. Although the size of glass beads is less than that of dolomite aggregates, glass beads are more rounded than dolomite aggregates, and the effect of particle size on the segregation behavior of the mixture is presumably overwhelmed by the effect of particle shape, such that relatively rounded glass beads, instead of relatively large dolomite aggregates, are more likely to move further, leading to the reverse sorting feature. In general, varying the shape of small particles from irregular to rounded seems to make the segregation curve rotate in an anti-clockwise direction around a certain pivot point. The particle density may not play a determining role in the reverse segregation of this test series because the absolute particle density difference for the two component materials is 0.32 g/cm^3, which is approximately 11% of the mean density value, and this difference is unlikely to give rise to a significant reverse sorting feature.

Table 5
Graphic Segregation Index (GPSI) Values in Different Test and Simulation Series

Category	Target effect	Test/ simulation name	Varying size/ shape factor	*GPSI* value
Test series	Size effect	II-G-B(a)	$d = 6\sim9$ mm	0.4846
		II-G-B(b)	$d = 10\sim20$ mm	0.4287
		II-G-B(c)	$d = 20\sim30$ mm	0.3064
	Shape effect	II-G-B(b)	$OR = 0.731$	0.4287
		II-G-S(b)	$OR = 0.746$	0.313
		II-G-D(b)	$OR = 0.764$	0.2046
Numerical series	Size effect	II-SS-FS(a)	$d = 15$ mm	0.8244
		II-SS-FS(b)	$d = 24$ mm	0.6667
		II-SS-FS(c)	$d = 32$ mm	0.5446
	Shape effect	II-SS-EG(c)	$OR = 0.673$	0.6366
		II-SS-FS(c)	$OR = 0.735$	0.5446
		II-SS-TS(c)	$OR = 0.869$	0.4636

Figure 6a shows the segregation profiles for the simulation series of I-TS-SS(a), I-TS-SS(b) and I-TS-SS(c), in which the binary mixtures are composed of tetrahedral (named "TS") shaped (base material) and spherical (referred to as "SS") particles of varying size ($d = 24$ mm, 32 and 50 mm) (addition material). Other material abbreviations in the simulation series are accessible from Table 4. The particle size of the base material is $d = 15$ mm. The segregation profiles show the same variation trend as observed in experiments (see Figure 5a) and have the same implications for the distribution of particles. With an increase in the size of spherical particles, the profile curve section for the slope part near the slope crest tends to rise, and the section for the distal slope part (near the slope toe) tends to dip, meaning that increasing the size of spherical particles makes more of them move to the lower part and induces a more marked segregation phenomenon.

The segregation profiles for the simulation series of I-TS-ES(a), I-TS-SR(a) and I-TS-SS(a) are shown in Figure 6b. The constituent particles of addition materials have different particle shapes, and the *OR* values are 0.7712 and 0.7816, respectively, for the ellipsoid and subrounded shapes, which are smaller than $OR = 1.0$ for the spherical shape. The particle size ($d = 15$ mm) for the base material is less than that ($d = 24$ mm) for the three addition materials. Figure 6b shows that the reduction of particle shape irregularity for addition materials enhances the segregation degree since the curve section for the upper part is the highest, and that the lower part is the lowest for the case of I-TS-SS(a). This phenomenon also supports the experimental finding that relatively rounded and large particles are prone to move further and settle near the toe of deposits.

## 3.2. Particle Sorting (Segregation) Analysis

For a quantitative analysis of the sorting feature, a novel segregation index proposed by Dai et al. (2020), the graphic segregation index (*GPSI*), is used to characterize the degree of sorting of deposited mixtures. The *GPSI* value for a normal segregation state ranges from 0 to 1.0, with 0 referring to a complete mixing state and 1.0 representing the state of full normal segregation (i.e., relatively large particles deposit at the lower part, and relatively small ones are in the upper part). The index value for a reverse segregation state varies from −1.0 to 0, with −1.0 denoting the state of full reverse segregation, at which relatively small particles accumulate in the lower part of the board and relatively large particles settle in the upper part.

Table 5 compares the *GPSI* values by considering the test series of II-G-B(a), II-G-B(b), and II-G-B(c), in which the base material is glass beads with $d = 25$ mm, and the addition materials are basalt aggregates of three size levels (i.e., $d = 6\sim9$ mm, 10∼20 mm, and 20∼30 mm). The *GPSI* value decreases with an increasing particle size of basalt aggregates, which indicates that increasing the particle size of basalt aggregates promotes the probability of their migrating downwards and leads to the mitigation of segregation degree. Table 5 also shows the *GPSI* values for the tests of II-G-B(b), II-G-S(b), and II-G-D(b), with the base material being glass beads ($d = 25$ mm) and the addition material having various shapes ($d = 10\sim20$ mm). The promotion of irregularity in particle shape for addition materials enhances the segregation degree of deposited mixture; that is, the more irregular the grain shape of addition materials (with a relatively small particle size), the more addition materials accumulate near the initial point of impact.

The *GPSI* values for the cases in the simulation series with the addition materials of various particle sizes (i.e., II-SS-FS(a), II-SS-FS(b), and II-SS-FS(c)) and of different particle shapes (i.e., II-SS-EG(c), II-SS-FS(c) and II-SS-TS(c)) are shown in Table 5. In two series of simulation cases, the base material is made up of spherical particles that have a larger particle size (i.e., $d = 50$ mm) than the constituent particles for all addition materials. The *GPSI* value decreases with both increasing particle size and shape factor *OR* of addition materials, and this result is consistent with the experimental finding. Both the experimental and simulation results suggest that the narrowing of the difference in particle size and shape between the base and addition materials tends to induce a weaker segregation phenomenon.
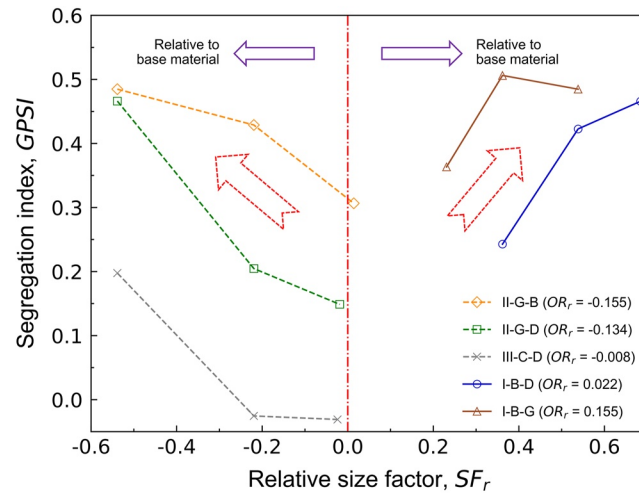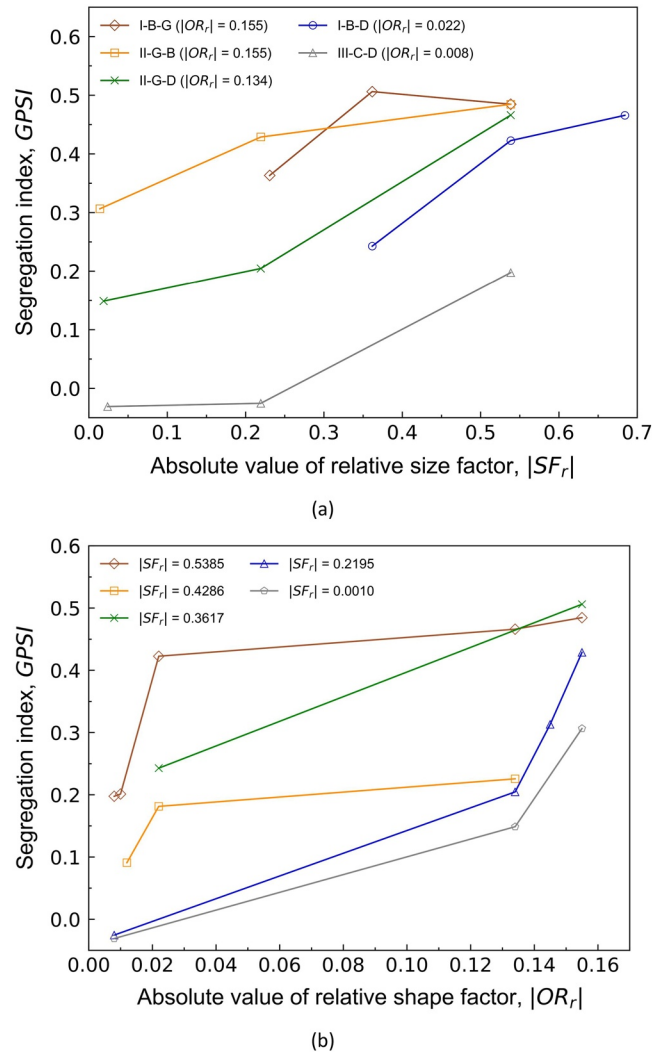
(a)
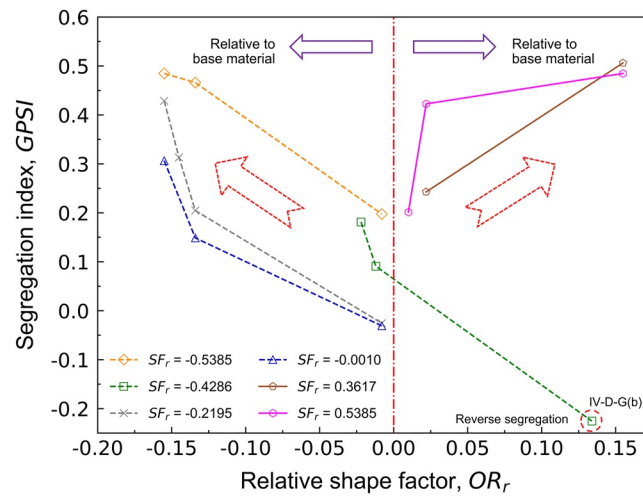
(b)

Figure 7. Relations of graphic segregation index (*GPSI*) with relative particle size and shape factors: (a) *GPSI* versus relative size factor (*SF*r); (b) *GPSI* versus relative shape factor (*OR*r).

Now, we introduce the relative size and shape factors to characterize the size and shape difference for a closer examination of sorting, with the expressions given as:

$$\text{Relative size factor} : SF_r = \frac{\overline{d}_a - \overline{d}_b}{\overline{d}_a + \overline{d}_b} \tag{2}$$

$$\text{Relative shape factor} : OR_r = \frac{OR_a - OR_b}{OR_a + OR_b} \tag{3}$$

where $\overline{d}_a$ and $\overline{d}_b$ are the average particle sizes for the addition and base materials, respectively; and OR_a and OR_b are the factors of overall regularity for the addition and base materials, respectively. Figure 7a shows that *GPSI* is positively correlated with the relative size factor SF_r if SF_r and OR_r are both positive, and that it has a negative correlation with SF_r in case SF_r and OR_r are both negative. Given that the addition materials have more irregular particle shapes ($OR_r < 0$) and smaller particle sizes ($SF_r < 0$), increasing the particle size discrepancy (i.e., decreasing SF_r) between the base and addition materials enhances the segregation degree (i.e., the *GPSI*

Figure 8. Relations of graphic segregation index (*GPSI*) with absolute values of relative particle size and shape factors for test series: (a) *GPSI* versus relative size factor (|*SF*$_r$|); (b) *GPSI* versus relative shape factor (|*OR*$_r$|).

value). If the addition materials have more regular particle shapes ($OR_r > 0$) and larger particle sizes ($SF_r > 0$), increasing the size difference (i.e., increasing SF_r) also promotes the segregation degree. Figure 7b shows a similar relationship between the *GPSI* index and the relative shape factor OR_r: the increase in the particle shape difference between the base and addition materials increases the *GPSI* value and segregation degree. However, Figure 7b shows a reverse segregation case (i.e., IV-D-G(b)) with a notable negative *GPSI* value. The *GPSI* value in the test series of $SF_r = -0.4286$ shows an overall decreasing trend with OR_r. Concerning the reverse segregation case, we are still able to conclude that when OR_r is positive, decreasing the shape irregularity (i.e., Increasing the OR_r value) promotes the segregation degree because the absolute value of *GPSI* for the case of IV-D-G(b) has increased.

For ease of comparison, we redrew Figure 7 with the absolute values of the relative size and shape factors |*SF*$_r$| and |*OR*$_r$|, as shown in Figure 8. In terms of the case of IV-D-G(b), we use a positive *GPSI* value to characterize the segregation degree. Figure 8 shows that *GPSI* increases with the absolute values of relative size and shape factors, |*SF*$_r$| and |*OR*$_r$|. In the same manner, Figure 9 plots the *GPSI* values against the absolute values of relative size and shape factors, |*SF*$_r$| and |*OR*$_r$|, for all numerical cases. The correlations of the *GPSI* value (i.e., segregation degree) with the factors |*SF*$_r$| and |*OR*$_r$| are in an overall good agreement with the observations in Figure 8. These
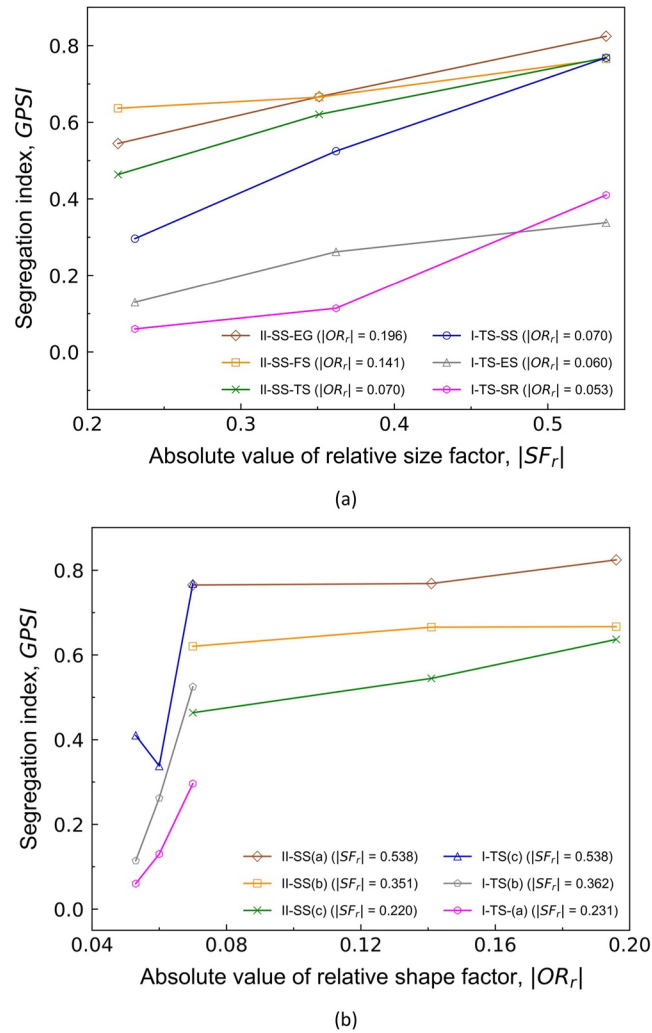
Figure 9. Relations of graphic segregation index (*GPSI*) with absolute values of relative particle size and shape factors for numerical cases: (a) *GPSI* versus relative size factor ($|SF_r|$); (b) *GPSI* versus relative shape factor ($|OR_r|$).

observations further support the finding that the larger the difference in particle size (or shape) between the base and addition materials is, the higher the degree of particle size (or shape) segregation.

4. Micromechanical Analysis

4.1. Particle Migration Mode

The fundamentals underlying the particle sorting phenomenon follow Newtonian mechanics. To scrutinize particle sorting in more detail, we set a number of tracer particles and monitored the motions and energies of such particles in the numerical simulations. Figure 10a shows the variation in kinetic energy normalized by particle mass (i.e., $E_{kn} = E_k/m$) with elapsed time t by focusing on two tracer particles at a certain particle releasing and accumulating process, wherein E_k is the kinetic energy composed of the translational and rotational parts that can be expressed as $(mv^2 + J\omega^2)/2$. The normalized kinetic energies for the two modeled particles demonstrate an overall declining tendency. Particle motions are also shown to evolve at a special mode before they stop, which is characterized by a general process of "initial falling → collision/friction ⇌ regaining ⇌ collision/friction → eventual rest state." After the release of the mixture from the hopper, particles typically acquire a high velocity immediately before their initial contact with the board. After the first collision with the bed, the particles tend
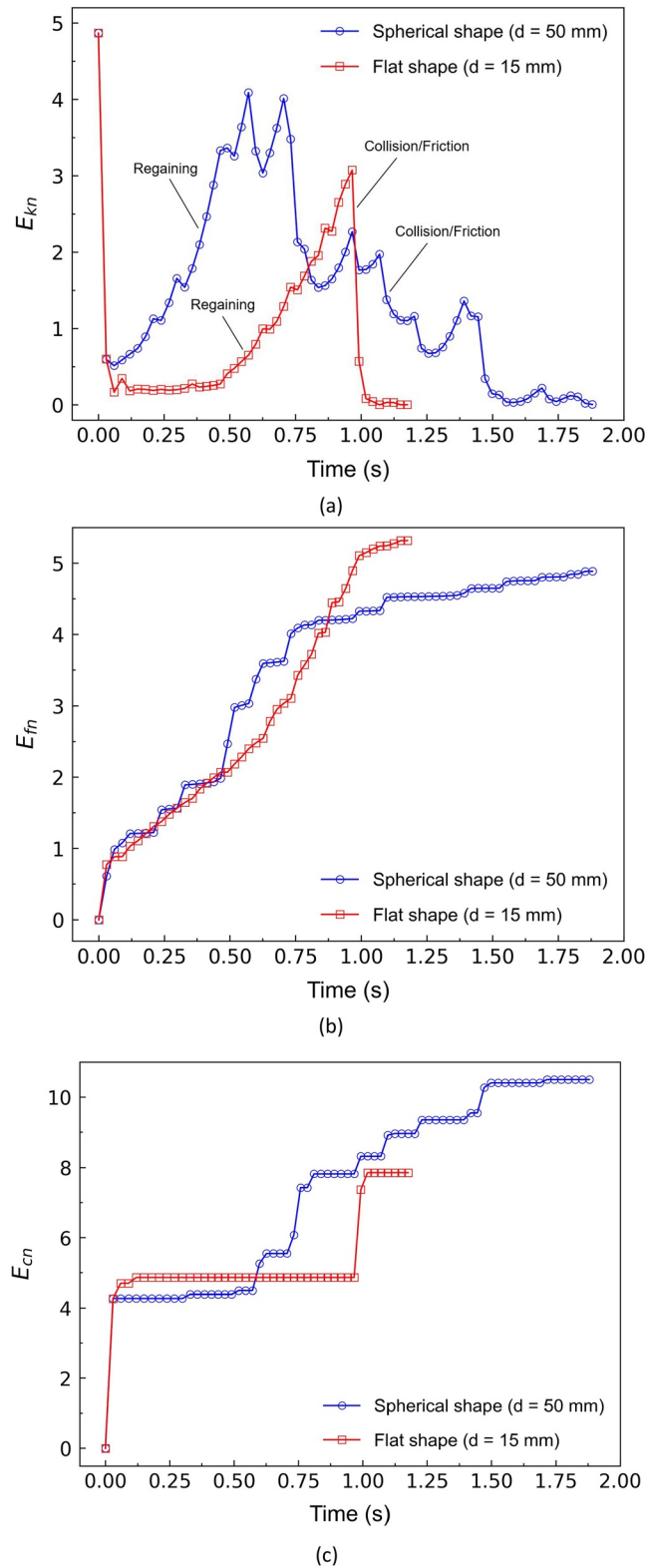
Figure 10. Evolution of (a) kinetic energy, (b) friction energy consumption, and (c) collision energy consumption of the tracer particles during the 14th release for the case of II-SS-FS(a).

to lose most of the kinetic energy, with E_{kn} decreasing markedly in the initial state. However, the particles are expected to regain kinetic energy in the next descending process due to the contribution of work done by gravity against frictional forces. In the next migration process, particles periodically undergo the process of "collision/friction ⇌ regaining ⇌ collision/friction" until they come to rest.

As shown in Figure 10a, the kinetic energy of the large and spherical particles is dissipated at a relatively slow rate compared to the small and irregular particles, indicating that large and round particles are more likely to move further within a relatively long period of time, and the motions of small and irregular particles may soon be stopped at a comparatively small migration distance. That is, the kinetic energy dissipation rate plays a key role in the particle migration distance.

In Figure 10b and Figure 10c, we present the evolutions of the normalized friction energy consumption (i.e., $E_{fn} = E_f/m$) and collision energy consumption (i.e., $E_{cn} = E_c/m$). Figure 10b shows that the friction energy consumption experiences a steady increase for the two component particles during their migration, and the frictional dissipation for the small and irregular particles is faster. Figure 10c shows that the collision dissipation depends on several major collisions during migration. The large and spherical particles suffer from more collisions than the small and irregular particles.

4.2. Kinetic Energy Dissipation Rate

As discussed above, the energy dissipation rate is a critical indicator of particle migration distance, which determines particle segregation. Thus, we introduce the dissipation rate of kinetic energy, D_k, which is defined as:

$$D_k = \frac{dE_{kn}}{dt} \tag{4}$$

The kinetic energy dissipation rate is given by the incremental kinetic energy within a time increment divided by this time increment (approximately 0.03 s), which is equivalent to 1,000 time steps in the DEM program. For ease of comparison, a given migration moment is normalized by the relatively long motion period for one of the tracer particles to give a normalized migration moment. Figure 11 shows the variations in the kinetic energy dissipation rates of the two tracer particles for the cases of II-SS-FS(a) and II-SS-TS(a) against the normalized time. Some highly scattered data points exist and are indicative of high kinetic energy dissipation rates. These scattered points may be linked with collision behavior, which contributes to considerable energy loss.

Figure 12 shows the best-fit curves of the raw data for a more in-depth inspection. The (absolute) kinetic energy dissipation rate exhibits an overall decreasing trend; that is, the kinetic energy dissipation rate decreases as particles move downwards along the board and approaches zero when they cease to migrate. The energy dissipation rate for the large and rounded particles is also lower than that for the small particles of irregular shape, which explains the observation in Figure 10a that relatively large and rounded particles tend to travel farther within a longer migration period.

4.3. Relation of the Kinetic Energy Dissipation Rate With Particle Properties

To compare the kinetic energy dissipation rates of component materials in the mixture in more detail, we propose the index of the relative kinetic energy dissipation rate between the addition and base materials, $|D_{k\_r}|$, which is defined as:

$$|D_{k\_r}| = \frac{|\overline{D}_{k\_a} - \overline{D}_{k\_b}|}{|\overline{D}_{k\_a} + \overline{D}_{k\_b}|} \tag{5}$$
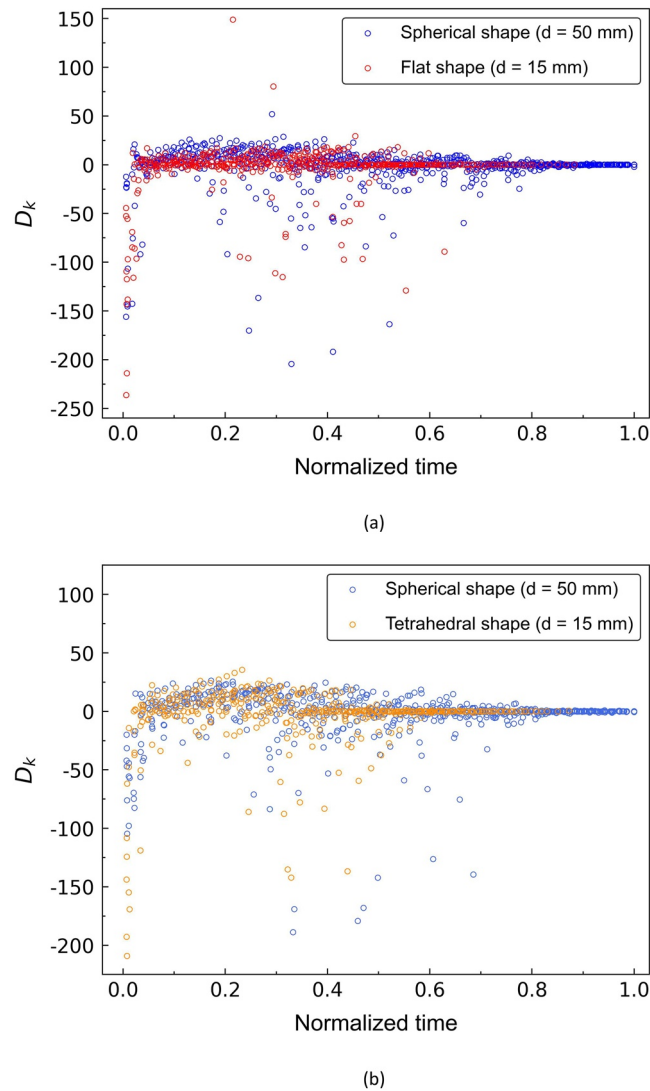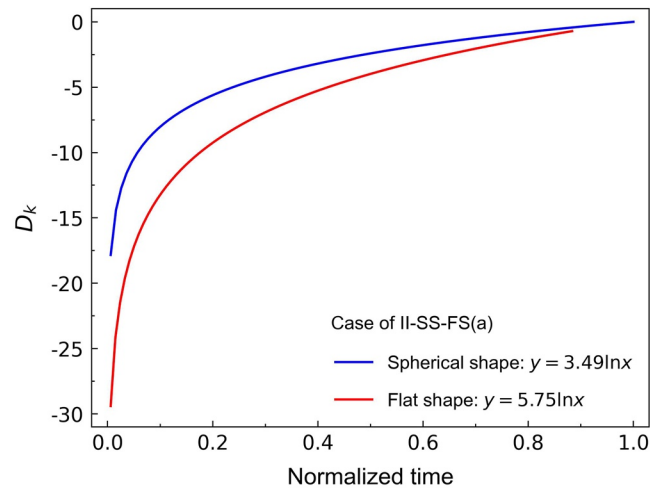
Figure 11. Evolution of kinetic energy dissipation rates for the tracer particles: (a) spherical and flat shapes in II-SS-FS(a); (b) spherical and tetrahedral shapes in II-SS-TS(a).

where $\overline{D}_{k\_a}$ and $\overline{D}_{k\_b}$ refer to the mean kinetic energy dissipation rates for the addition and base materials in a given simulation case, respectively. Figure 13 compares $|D_{k\_r}|$ and *GPSI* by focusing on the influence of particle size and shape. The particle size for the addition material is varied in the series of II-SS-EG(a), II-SS-EG(b), and II-SS-EG(c), and the particle shape is different for the addition material in the series of II-SS-EG(a), II-SS-FS(a), and II-SS-TS(a). Particles for the base materials in these two series are spherical, and their sizes ($d = 50$ mm) are larger than those ($d = 15$ mm, 24 and 32 mm) for the addition materials.

Figure 13 shows that $|D_{k\_r}|$ generally decreases with increasing particle size and shape factor *OR* for the addition materials, as does the *GPSI* index, meaning that $|D_{k\_r}|$ decreases as the difference in particle size and shape decreases. Figure 13 also shows that $|D_{k\_r}|$ is positively correlated with *GPSI*, indicating that the sorting phenomenon depends on the relative kinetic energy dissipation rate between the component materials. In general, the larger the relative kinetic energy dissipation rate is, the higher the degree of segregation.

(a)
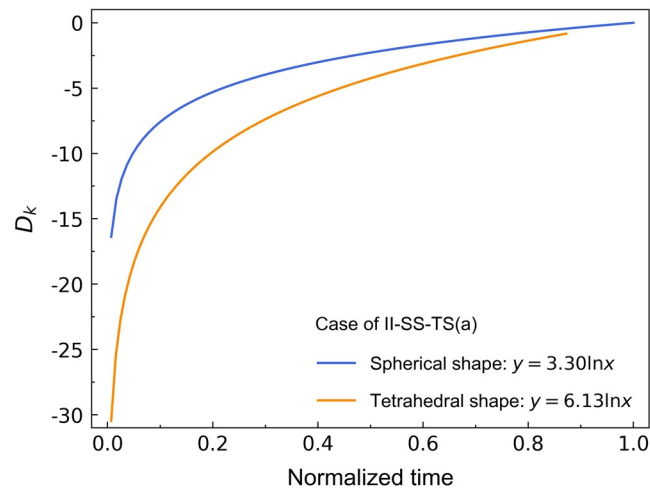
(b)

Figure 12. Best-fit curves of kinetic energy dissipation rates for the tracer particles in the cases of (a) II-SS-FS(a) and (b) the case of II-SS-TS(a).

We plot the relative kinetic energy dissipation rate in Figure 14 with respect to the absolute values of the relative particle size and shape factors, $|SF_r|$ and $|OR_r|$. The relations of $|D_{k\_r}|$ with the factors of $|SF_r|$ and $|OR_r|$ are comparable to those for the *GPSI* values, as shown in Figures 8 and 9. That is, $|D_{k\_r}|$ increases as $|SF_r|$ and $|OR_r|$ increase, except for some individual cases. This observation agrees with the finding from Figure 13 that the segregation degree has a positive correlation with the relative kinetic energy dissipation rate.

Thus, the promotion of the discrepancy in particle size and shape between the component materials of the binary mixture leads to the escalation of the difference in their kinetic energy dissipation rates (i.e., an increase in the relative kinetic energy dissipation rate $|D_{k\_r}|$). An increasing difference in the kinetic energy dissipation rate is responsible for a more noticeable differentiation between the migration distances of the two component materials, resulting in a stronger sorting (segregation) phenomenon.
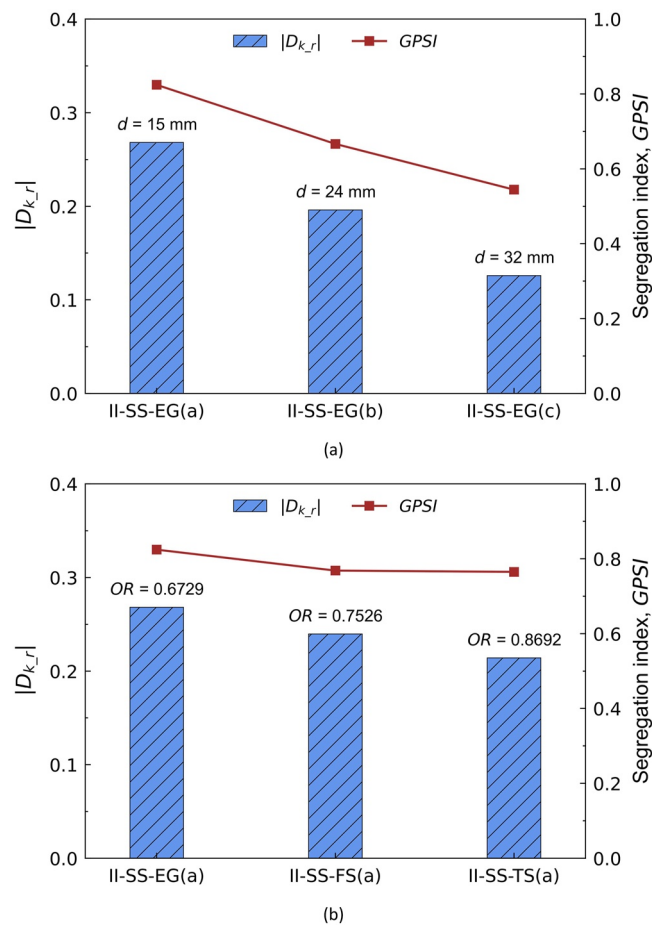
Figure 13. Relations of the relative kinetic energy dissipation rate $|D_{k\_r}|$ and graphic segregation index (*GPSI*) with particle size and shape for (a) the simulation series of II-SS-EG(a), II-SS-EG(b), and II-SS-EG(c) and (b) the simulation series of II-SS-EG(a), II-SS-FS(a), and II-SS-TS(a).

5. Discussion

5.1. Mechanism Accounting for the Effect of Particle Size and Shape on the Kinetic Energy Dissipation Rate
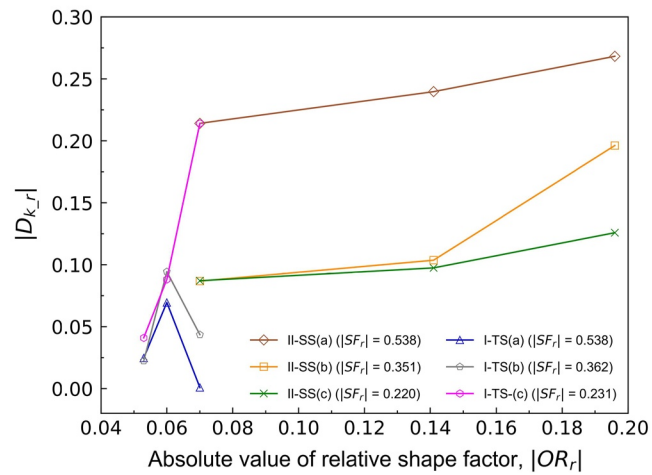
The effect of the relative particle shape and size factor on the relative kinetic energy dissipation rate is assumed to depend on the energy dissipation mode of particles during migration. Given two particles with the same size but different shapes, the more rounded particle tends to experience more rolling behavior than the more irregular particle. The particle rolling resistance is typically less than the particle sliding resistance, and thus, the kinetic dissipation rate of the relatively rounded particle is considered to be lower.

For two particles with the same shape but different sizes, it is easier for the relatively large particle to overcome resistance during migration and move over the accumulated mass. It is more difficult for the relatively small particle to overcome the resistance induced by the asperity of the top surface of the accumulated mass due to the disparity of particle size and surface relief (see Figure 15); thus, a relatively small particle experiences a larger resistance compared to its kinetic energy and tends to be trapped in voids or gaps. In this connection, the kinetic energy dissipation rate for a relatively small particle is comparatively high.

Given that two particles share the same initial kinematic state, the relatively small or irregular particle experiences a relatively high energy dissipation rate and takes a shorter period of time to complete the migration. Thus, the migration distance for a small/irregular particle is less than that for a large/rounded particle. The sorting mechanism revealed in this study is supported by a number of field observations from scree slopes in North
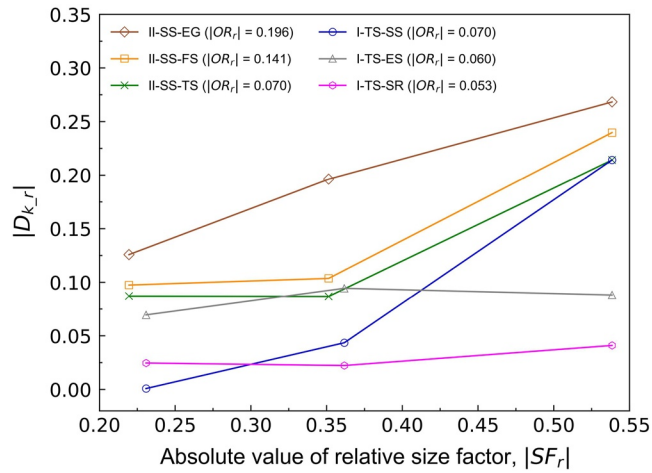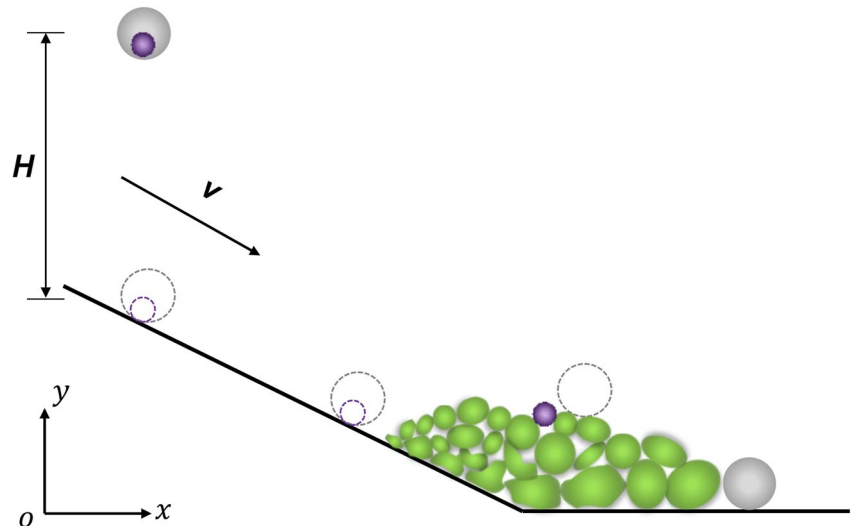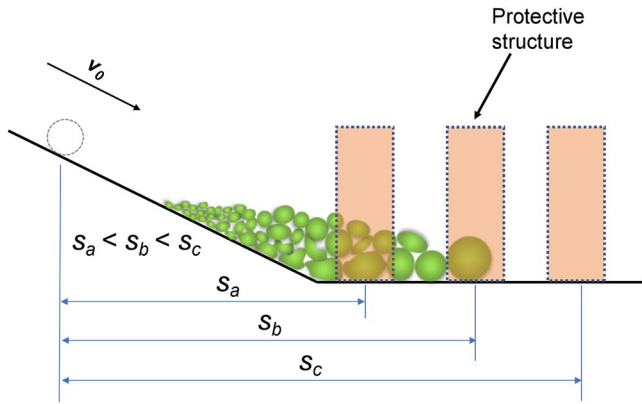
Figure 14. Relations of the relative kinetic energy dissipation rate with absolute values of relative particle size and shape factors for numerical cases: (a) $|D_{k\_r}|$ versus $|SF_r|$; (b) $|D_{k\_r}|$ versus $|OR_r|$.

Figure 15. Schematic description of the effect of particle size on the kinetic energy dissipation rate.

Figure 16. Schematic illustration of the effect of particle motion on the protective structure.

America, Europe and northwestern China (e.g., Gardner, 1970; Sass, 2006; Zhang et al., 2010). The scree slopes in high-frigid mountainous regions without the influence of vegetation, snow avalanches and glacier movement may tend to show the particle sorting feature which could be explained by the mechanism revealed in this study.

However, there still exist some exceptional cases in which limited sorting, no sorting, or even reverse sorting is observed (e.g., Bones, 1973; Caine, 1967, 1969; De Blasio & Sæter, 2010; De Scally & Owens, 2005; Gardner, 1968; Haas et al., 2012; Jomelli & Francou, 2000; Luckman, 1971; Pérez, 1985; Thornes, 1971). This is because the formation and evolution processes of scree slopes are complex in reality, and in addition to the size and shape of rock fragments, they are also governed by a number of other factors (e.g., slope angle, bedrock type, vegetation, surface roughness) (Caine, 1969; Haas et al., 2012; Pérez, 1998). Also, geomorphic and geological processes (e.g., glacier advance, snow avalanche, debris flow, streamflow) play critical roles in scree slope formation and evolution (Curry & Morris, 2004; De Scally & Owens, 2005; Jomelli & Francou, 2000; Luckman, 1971) and thus exert an influence on the characteristics of slope deposits. For example, vegetation may serve as an obstacle to prevent rock fragments from moving downwards from the slope (Pérez, 1998), and snow avalanches or glacier advances may help erase the original fabric of slope deposits (Curry & Morris, 2004; De Scally & Owens, 2005; Jomelli & Francou, 2000). It is important to consider that the combined effect of such factors can contribute to the complex sorting feature in real scree slopes.

5.2. Implication for the Configuration of Protective Structures

It is important to properly configure protective structures for hazard prevention. Protective structures can help attenuate the impact of coarse particles and reduce the final run-out of granular flows (Iverson et al., 2016; Mancarella & Hungr, 2010; Ng et al., 2021; Yang et al., 2021). The design of protective structures should consider a number of factors (Lei et al., 2020; Li et al., 2010; Liu et al., 2021; Salciarini et al., 2010), including slope length, slope angle, granular flow mass, and particle size distribution. Lei et al. (2020) show that an increase in the number of baffle rows leads to an increase in coarse particles retained by the baffles, referring to the grain size variation at different locations of debris deposits; that is, particle sorting plays an important role in protective structure design. This section thus provides a preliminary discussion of the role of particle sorting in the configuration of protective structures. As shown in Figure 16, larger and more rounded particles tend to move further to the distal part of the slope at a comparatively lower kinetic energy dissipation rate, meaning that protective structures are primarily subjected to the impact from large particles.

We assume that a particle moves downwards with the initial velocity v_0 and its migration distance is S_0 without the presence of protective structures. If a protective structure is present, the impact force depends on the kinetic energy of the moving particle at the moment when it arrives at the protective structure:

$$F \propto E_{k\_f} = \beta_f m v_f^2 \tag{6}$$

where v_f is the particle velocity when the particle impacts the protective structure, and β_f is a kinetic energy coefficient considering both the translation and rotation behavior. If the time required for the particle to reach the structure is t, the kinetic energy can be described by

$$E_{k\_f} = \beta_f m v_f^2 = E_{k\_ini} - m \int_0^t D_k \mathrm{d}t = \beta_0 m v_0^2 - m \int_0^t \lambda \ln t \mathrm{d}t \tag{7}$$

where D_k is the kinetic energy dissipation rate; β_0, similar to β_f, is a kinetic energy coefficient for the initial state; λ, as indicated in Figure 12, is a coefficient related to the particle properties and is relatively low for large and rounded particles.

Given that the distance between the falling point and the protective structure is S, small particles typically have a high kinetic energy dissipation rate and are expected to have relatively low kinetic energies when they reach the
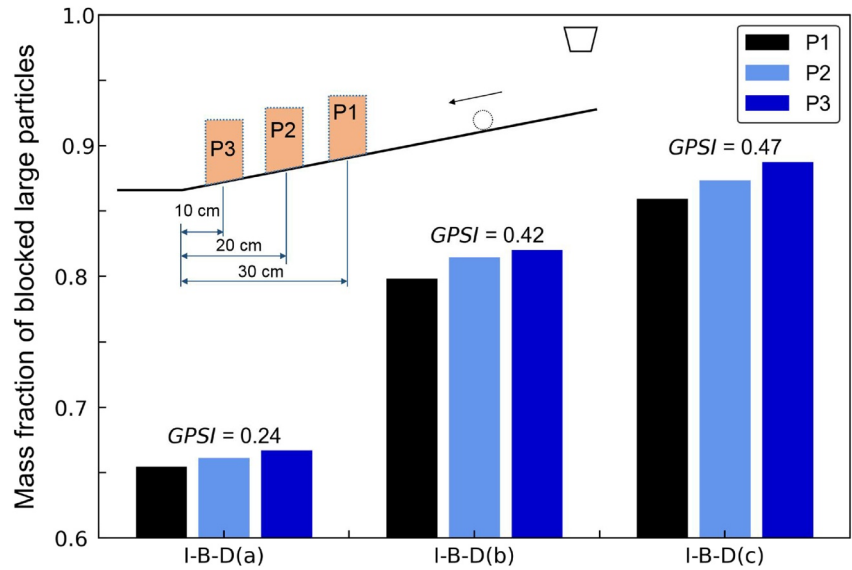
Figure 17. Relations of the mass fraction of large particles blocked by protective structures with particle size, considering different protective structure positions, for the test series of I-B-D(a), I-B-D(b), and I-B-D(c).

protective structure, or they may not be able to move the distance S and thus do not impact the protective structure. Large particles have relatively high kinetic energies when they arrive at the protective structure. In general, the distance S should not be much larger than the S_0 of large particles. A large S (e.g., S_c in Figure 16) may not be able to fully mobilize the targeted function of structures or even make the structures lose their value, while a small S (e.g., S_a in Figure 16) may overburden the structures. It is therefore critical to use an appropriate S (e.g., S_b in Figure 16) in practice to maximize the protection effect of defending structures and ensure their security and stability.

For a quantitative evaluation of the effect of particle sorting, we assume that a protective structure is placed at three proper positions (i.e., P1, P2, and P3), as indicated by the inset in Figure 17, along the slope of the apparatus in this study, and the particles behind the protective structure should be blocked. Following this assumption, we estimate the mass proportion of blocked large particles in the entire blocked mass by focusing on the test series of I-B-D(a), I-B-D(b), and I-B-D(c). The design of a protective structure requires the consideration of the earth pressure induced by the blocked mass, as well as the impact forces of particles when they collide with the protective structure. A higher proportion of large particles in the blocked mass means that the protective structure will be subjected to higher impact forces and is more prone to fail. It is thus reasonable to infer that a correlation between the impact effect of moving particles on the protective structure and the degree of particle sorting in scree slopes exists.

By concentrating on three experiments in a particular series, Figure 17 shows the mass fractions of blocked large particles at different positions, where P1 is nearest to the particle release source and P3 is the farthest. We find that the mass fraction of blocked large particles at P1 is the lowest, but the earth pressure is supposed to be the largest because P1 is the nearest to the release source and the blocked mass should be the largest. At a given position, the mass fraction of obstructed large particles increases with an increasing *GPSI* value, which means that a more pronounced sorting phenomenon is responsible for a higher impact effect of large particles on the protective structure, which must be considered in the design of protective structures.

6. Concluding Remarks

We have performed a series of physical model experiments and DEM simulations to systematically examine the particle sorting feature in scree slopes and to provide a quantitative explanation of the involved fundamentals by scrutinizing the particle migration and energy dissipation from a micromechanical perspective.

Particle characteristics such as particle shape and size play an essential role in the occurrence of the sorting phenomenon in scree slope deposits: relatively round and large particles tend to travel farther to accumulate at the distal part of the slope, and relatively small and irregular particles are prone to settle in the upper part of the

slope. The sorting (segregation) degree increases with increasing size and shape difference between the constituent materials. With the introduction of the relative size and shape factors, SF_r and OR_r, we identified a positive correlation between the segregation index $GPSI$ and the absolute values of the relative size and shape factors $|SF_r|$ and $|OR_r|$.

The migration of particles is shown to occur in a periodical motion mode of "collision/friction $\rightleftharpoons$ regaining $\rightleftharpoons$ collision/friction" until the rest state is finally reached. Energy analyses indicate that the kinetic energy dissipation rate of particles generally decreases as particles move downwards and that the relatively large and rounded particles travel downwards with a lower kinetic energy dissipation rate and take a longer period of time to accomplish a larger migration distance.

The relative kinetic energy dissipation rate $|D_{k\_r}|$ is found to have a positive correlation with the relative particle size and shape factors, $|SF_r|$ and $|OR_r|$. An increasing discrepancy in particle size and shape between the component materials of the deposited mixture leads to an increase in the difference in their kinetic energy dissipation rates and thus induces a more marked distinction in the travel distances of the two component materials and a more notable sorting feature.

Appendix A: Shape Factors

The indices of convexity (C), roundness (R), and aspect ratio (AR) are used to characterize the particle shape. As shown in Figure A1a, the convexity is given by the ratio of the diameter of the largest inscribed circle (sphere) centered in the center-of-mass of the particle to the diameter of the smallest circumscribed circle (sphere):

$$C = \frac{D_{\text{inscrib\_max}}}{D_{\text{circum\_min}}} \tag{A1}$$

The roundness, which is also referred to as circularity, is the ratio of the perimeter squared to the projected area times 4π for a given particle:

$$R = \frac{P^2}{4\pi A_P} \tag{A2}$$

where P is the perimeter of a particle and A_P is the projected area. According to Equation A2, the roundness is also interpreted as the square of the perimeter ratio between a given particle and a circular particle with an equivalent area (Dai et al., 2017). Similarly, the sphericity for a 3D case is defined as the squared ratio of the volume-equivalent and surface-equivalent diameters:

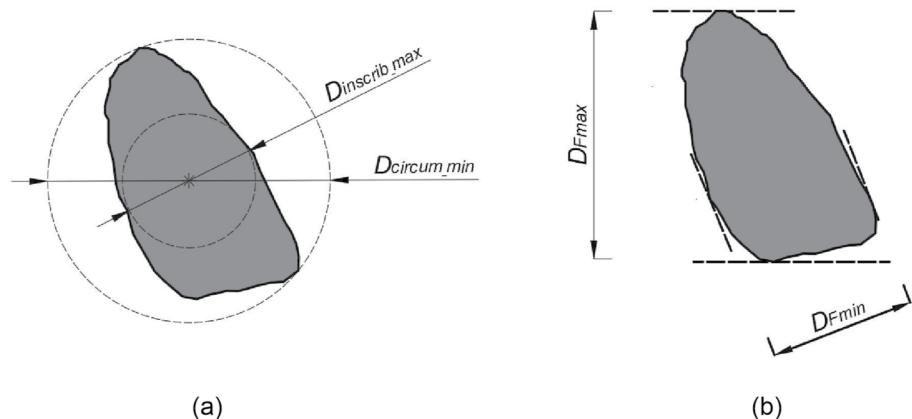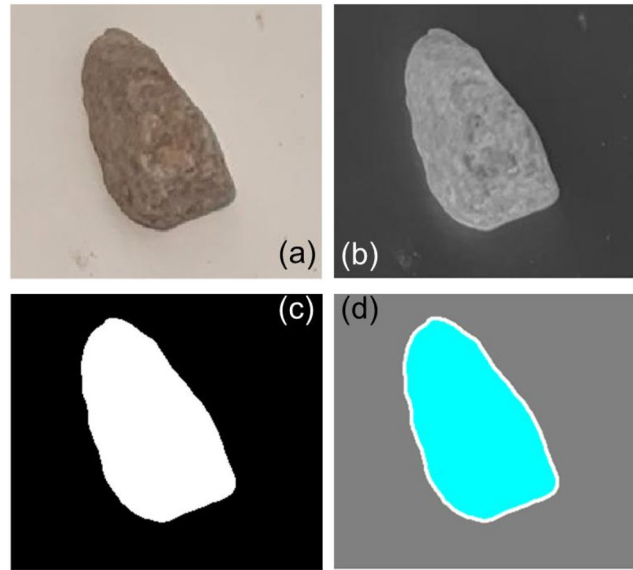$$S = \left(\frac{D_V}{D_S} \right)^2 \tag{A3}$$

(a)　　　　　　　　　　　　　　(b)

Figure A1. Description of shape factors.

Figure A2. Description of image processing.

where D_V and D_S are the diameters of volume-equivalent and surface-equivalent particles, respectively.

The aspect ratio of a particle is defined as the ratio between the minimum and maximum Feret diameters, as shown in Figure A1b (Cavarretta et al., 2010; Pabst & Gregorova, 2007; Yang & Luo, 2015; Yang & Wei, 2012):

$$AR = \frac{D_{Fmin}}{D_{Fmax}} \tag{A4}$$

For image processing, first, we randomly choose 10 grains as representative sample grains for a specific material and take a photo for each sample grain. Then, we load the picture file into MATLAB, read the raw image data and convert the original image to a greyscale image (see Figures A2a and A2b). Third, we binarize the converted image and identify the particle boundary (see Figures A2c and A2d). Finally, we determine based on the processed image, the shape factors of aspect ratio (*AR*), convexity (*C*) and roundness (*R*), as well as the overall regularity (*OR*) in Equation 1.

Appendix B: Graphic Segregation Index

Figure B1 shows the segregation profiles of three typical segregation states for a granular bed composed of both large and small particles during the segregating process: the initial fully-mixed state, the interim segregating state and the eventual completely-segregated state. The segregation profile for the fully-mixed state is a horizontal line (i.e., the line *AB*), meaning that the mass fraction of the small particles is a constant P_0. At the completely-segregated state, the small particles are supposed to be at the bottom part, and the large ones are at the upper part, with the segregation profile being the three line segments (i.e., lines *CD*, *DE*, and *EF*). The vertical line *DE* signifies the interface between the small and large particles. The curve *CF* is the segregation profile for an interim segregating state. During the segregation process, the segregation profiles are assumed to evolve from the initial horizontal line *AB* to the final pattern of three line segments *CD*, *DE* and *EF* in the form of curve *CF*. The evolution of segregation profiles is in fact accompanied by the variation of the area S_{mg} enclosed between the curve *CF* and line *AB*, with the lines *AC* and *BF* being the lateral boundaries. The segregation degree can be characterized by the ratio of the area S_{mg} to the enclosed area S_{fg} between the three line segments (i.e., lines *CD*, *DE*, and *EF*) and line *AB*. Thus, this ratio is defined as a segregation index *GPSI*:

$$GPSI = \frac{S_{mg}}{S_{fg}} \tag{B1}$$
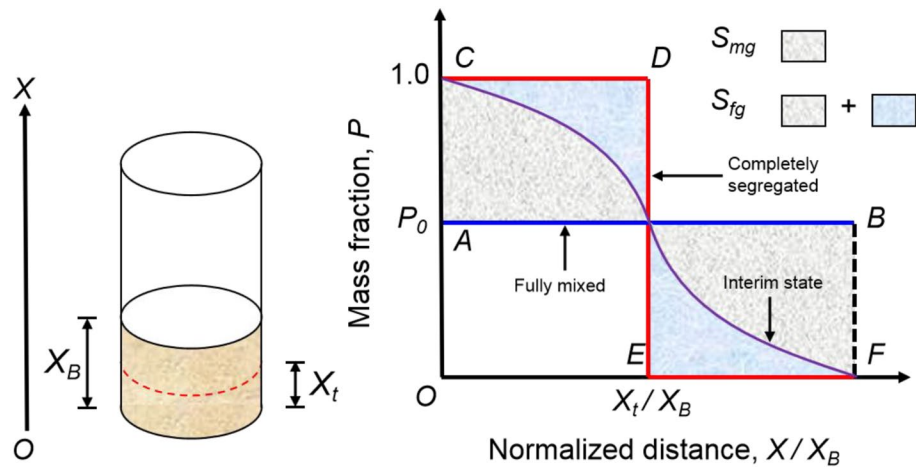
Figure B1. Segregation profiles at the fully-mixed state and completely-segregated states, as well as at an interim segregating state.

where S_{mg} is the enclosed area between the interim segregation profile curve *CF* and the line *AB* representing a fully-mixed state, and S_{fg} is the enclosed area between the line *AB* and the three line segments referring to a completely-segregated state. The segregation index *GPSI* equals 0 at the fully-mixed state and equals 1.0 at the fully-segregated state.

The interim segregation profile is assumed to be an idealized curve that passes through the intersection point of lines *AB* and *DE*. In reality, the interim segregation profile could be more complex than this assumed pattern because the segregation of particles may not proceed in an even and progressive manner. To capture the real complex segregation features, *GPSI* has also been modified by considering the occurrence of reverse segregation. One may consult Dai et al. (2020) for the details, and we do not introduce them in this study due to the length limits of this article.

Data Availability Statement

We here declare that we comply with AGU's data policy. The data generated or analyzed in this study have been included in this article, and uploaded to Mendeley Data (https://data.mendeley.com/datasets/4bxmd5cfnb/1). There are no data from the literature or other sources, the access of which requires a license or is restricted.

References

Bertran, P., Hétu, B., Texier, J. P., & Van Steijn, H. (1997). Fabric characteristics of subaerial slope deposits. *Sedimentology*, *44*, 1–16. https://doi.org/10.1111/j.1365-3091.1997.tb00421.x

Bi, Y., He, S., Li, X., Ouyang, C., & Wu, Y. (2016). Effects of segregation in binary granular mixture avalanches down inclined chutes impinging on defending structures. *Environmental Earth Sciences*, *75*(3), 1–8. https://doi.org/10.1007/s12665-015-5076-1

Bithell, M., Richards, K. S., & Bithell, E. G. (2014). Simulation of scree-slope dynamics: Investigating the distribution of debris avalanche events in an idealized two-dimensional model. *Earth Surface Processes and Landforms*, *39*(12), 1601–1610. https://doi.org/10.1002/esp.3548

Bones, J. G. (1973). Process and sediment size arrangement on high arctic talus, southwest Devon Island, NWT, Canada. *Arctic and Alpine Research*, *5*(1), 29–40. https://doi.org/10.1080/00040851.1973.12003676

Caine, N. (1967). The texture of talus in Tasmania. *Journal of Sedimentary Research*, *37*(3), 796–803. https://doi.org/10.1306/74d717a3-2b21-11d7-8648000102c1865d

Caine, N. (1969). A model for Alpine talus slope development by slush avalanching. *The Journal of Geology*, *77*(1), 92–100. https://doi.org/10.1086/627410

Carson, M. A. (1977). Angles of repose, angles of shearing resistance and angles of talus slopes. *Earth Surface Processes*, *2*(4), 363–380. https://doi.org/10.1002/esp.3290020408

Cavarretta, I., Coop, M., & O'Sullivan, C. (2010). The influence of particle characteristics on the behaviour of coarse grained soils. *Géotechnique*, *60*(6), 413–423. https://doi.org/10.1680/geot.2010.60.6.413

Curry, A. M., & Morris, C. J. (2004). Lateglacial and Holocene talus slope development and rockwall retreat on Mynydd Du, UK. *Geomorphology*, *58*(1–4), 85–106. https://doi.org/10.1016/S0169-555X(03)00226-5

Dai, B. B. (2018a). Influence of particle size and gradation on the stress-dilatancy behavior of granular materials during drained triaxial compression: Discussion. *International Journal of Geomechanics, ASCE*, *18*(12), 07018018. https://doi.org/10.1061/(asce)gm.1943-5622.0001298

Dai, B. B. (2018b). Probing the boundary effect in granular piles. *Granular Matter*, *20*(1), 1–14. https://doi.org/10.1007/s10035-017-0775-9

Dai, B. B., Yang, J., Gu, X. Q., & Zhang, W. (2019). A numerical analysis of the equivalent skeleton void ratio for silty sand. *Geomechanics & Engineering*, *17*(1), 19–30. https://doi.org/10.12989/gae.2019.17.1.019

Dai, B. B., Yang, J., Liu, F. T., Gu, X. Q., & Lin, K. R. (2020). A new index to characterize the segregation of binary mixture. *Powder Technology*, *363*, 611–620. https://doi.org/10.1016/j.powtec.2020.01.005

Dai, B. B., Yang, J., & Luo, X. D. (2015). A numerical analysis of the shear behavior of granular soil with fines. *Particuology*, *21*(4), 160–172. https://doi.org/10.1016/j.partic.2014.08.010

Dai, B. B., Yang, J., & Zhou, C. Y. (2016). Observed effects of interparticle friction and particle size on shear behavior of granular materials. *International Journal of Geomechanics*, *16*(1), 04015011. https://doi.org/10.1061/(asce)gm.1943-5622.0000520

Dai, B. B., Yang, J., & Zhou, C. Y. (2017). Micromechanical origin of angle of repose in granular materials. *Granular Matter*, *19*(2), 24. https://doi.org/10.1007/s10035-017-0709-6

Dai, B. B., Yuan, W. H., Liu, J. K., Liu, F. T., & Chang, D. (2021). Estimating the segregation of a granular bed subjected to vibration in various modes. *Advanced Powder Technology*, *32*(5), 1450–1462. https://doi.org/10.1016/j.apt.2021.03.001

De Blasio, F. V., & Sæter, M. B. (2009). Small-scale experimental simulation of talus evolution. *Earth Surface Processes and Landforms*, *34*(12), 1685–1692. https://doi.org/10.1002/esp.1861

De Blasio, F. V., & Sæter, M. B. (2010). Properties of talus slopes composed of flat blocks. *Norsk Geografisk Tidsskrift–Norwegian Journal of Geography*, *64*(2), 85–93. https://doi.org/10.1080/00291951.2010.481198

De Blasio, F. V., & Sæter, M. B. (2015). Dynamics of grains falling on a sloping granular medium: Application to the evolution of a talus. *Earth Surface Processes and Landforms*, *40*(5), 599–609. https://doi.org/10.1002/esp.3655

De Haas, T., Braat, L., Leuven, J. R. F. W., Lokhorst, I. R., & Kleinhans, M. G. (2015). Effects of debris flow composition on runout depositional mechanism, and deposit morphology in laboratory experiments. *Journal of Geophysical Research: Earth Surface*, *120*(9), 1949–1972. https://doi.org/10.1002/2015JF003525

De Scally, F. A., & Owens, I. F. (2005). Depositional processes and particle characteristics on fans in the Southern Alps, New Zealand. *Geomorphology*, *69*(1–4), 46–56. https://doi.org/10.1016/j.geomorph.2004.11.021

DiBiase, R. A., Lamb, M. P., Ganti, V., & Booth, A. M. (2017). Slope, grain size, and roughness controls on dry sediment transport and storage on steep hillslopes. *Journal of Geophysical Research: Earth Surface*, *122*(4), 941–960. https://doi.org/10.1002/2016JF003970

Evans, S. G., & Hungr, O. (1993). The assessment of rockfall hazard at the base of talus slopes. *Canadian Geotechnical Journal*, *30*(4), 620–636. https://doi.org/10.1139/t93-054

Gabet, E. J. (2003). Sediment transport by dry ravel. *Journal of Geophysical Research*, *108*(B1), 2049. https://doi.org/10.1029/2001JB001686

Gabet, E. J., & Mendoza, M. K. (2012). Particle transport over rough hillslope surfaces by dry ravel: Experiments and simulations with implications for nonlocal sediment flux. *Journal of Geophysical Research*, *117*(F01019). https://doi.org/10.1029/2011JF002229

Gardner, J. (1968). *Debris slope form and process in the Lake Louise district: A high mountain area'. Unpubl* Doctoral dissertation, Ph. D. thesis. McGill University.thesis.

Gardner, J. (1970). Geomorphic significance of avalanches in the Lake Louise area, Alberta, Canada. *Arctic and Alpine Research*, *2*(2), 135–144. https://doi.org/10.2307/1550348

Gray, J. M. N. T., & Chugunov, V. A. (2006). Particle-size segregation and diffusive remixing in shallow granular avalanches. *Journal of Fluid Mechanics*, *569*, 365–398. https://doi.org/10.1017/S0022112006002977

Gray, J. M. N. T., & Kokelaar, B. P. (2010). Large particle segregation, transport and accumulation in granular free-surface flows. *Journal of Fluid Mechanics*, *652*, 105–137. https://doi.org/10.1017/S002211201000011X

Gray, J. M. N. T., & Thornton, A. R. (2005). A theory for particle size segregation in shallow granular free-surface flows. *Proceedings of the Royal Society A: Mathematical, Physical & Engineering Sciences*, *461*(2057), 1447–1473. https://doi.org/10.1098/rspa.2004.1420

Gu, X. Q., Hu, J., & Huang, M. S. (2015). K0 of granular soils: A particulate approach. *Granular Matter*, *17*(6), 703–715. https://doi.org/10.1007/s10035-015-0588-7

Gu, X. Q., Lu, L. T., & Qian, J. G. (2017). Discrete element modeling of the effect of particle size distribution on the small strain stiffness of granular soils. *Particuology*, *32*(006), 21–29. https://doi.org/10.1016/j.partic.2016.08.002

Haas, F., Heckmann, T., Wichmann, V., & Becht, M. (2012). Runout analysis of a large rockfall in the Dolomites/Italian Alps using LIDAR derived particle sizes and shapes. *Earth Surface Processes and Landforms*, *37*(13), 1444–1455. https://doi.org/10.1002/esp.3295

Iverson, R. M., George, D. L., & Logan, M. (2016). Debris flow runup on vertical barriers and adverse slopes. *Journal of Geophysical Research: Earth Surface*, *121*(12), 2333–2357. https://doi.org/10.1002/2016jf003933

Johnson, C. G., Kokelaar, B. P., Iverson, R. M., Logan, M., Lahusen, R. G., & Gray, J. M. N. T. (2012). Grain-size segregation and levee formation in geophysical mass flows. *Journal of Geophysical Research*, *117*(F01032). https://doi.org/10.1029/2011JF002185

Jomelli, V., & Francou, B. (2000). Comparing the characteristics of rockfall talus and snow avalanche landforms in an Alpine environment using a new methodological approach: Massif des Ecrins, French Alps. *Geomorphology*, *35*(3–4), 181–192. https://doi.org/10.1016/s0169-555x(00)00035-0

Kirkby, M. J., & Statham, I. (1975). Surface stone movement and scree formation. *The Journal of Geology*, *83*(3), 349–362. https://doi.org/10.1086/628097

Kotarba, A., & Strömquist, L. (1984). Transport, sorting and deposition processes of alpine debris slope deposits in the Polish Tatra Mountains. *Geografiska Annaler - Series A: Physical Geography*, *66*(4), 285–294. https://doi.org/10.2307/520851

Lei, M., Yang, P., Wang, Y. K., & Wang, X. K. (2020). Numerical analyses of the influence of baffles on the dynamics of debris flow in a gully. *Arabian Journal of Geosciences*, *13*(19), 1–15. https://doi.org/10.1007/s12517-020-06016-z

Li, X., He, S., Luo, Y., & Wu, Y. (2010). Discrete element modeling of debris avalanche impact on retaining walls. *Journal of Mountain Science*, *7*(3), 276–281. https://doi.org/10.1007/s11629-010-2019-x

Li, X., & Yu, H. S. (2010). Numerical investigation of granular material behaviour under rotational shear. *Géotechnique*, *60*(5), 381–394. https://doi.org/10.1680/geot.2010.60.5.381

Liu, R., Hua, D., & Chen, K. (2021). Experimental study on interaction between rock granular flow and different structural forms of rigid retaining walls. *Structures*, *34*, 3557–3566. https://doi.org/10.1016/j.istruc.2021.09.068

Lu, L. S., & Hsiau, S. S. (2008). DEM simulation of particle mixing in a sheared granular flow. *Particuology*, *6*(6), 445–454. https://doi.org/10.1016/j.partic.2008.07.006

Luckman, B. H. (1971). The role of snow avalanches in the evolution of alpine talus slopes. Slopes Form and Process. *Institute of British Geographers. Special Publication*, *3*, 93–109.

Mancarella, D., & Hungr, O. (2010). Analysis of run-up of granular avalanches against steep, adverse slopes and protective barriers. *Canadian Geotechnical Journal*, *47*(8), 827–841. https://doi.org/10.1139/t09-143

Martin, Y. (2000). Modelling hillslope evolution: Linear and nonlinear transport relations. *Geomorphology*, *34*(1–2), 1–21. https://doi.org/10.1016/S0169-555X(99)00127-0

McGrath, G. S., Nie, Z., Dyskin, A., Byrd, T., Jenner, R., Holbeche, G., & Hinz, C. (2013). In-situ fragmentation and rock particle sorting on arid hills. *Journal of Geophysical Research: Earth Surface*, *118*(1), 17–28. https://doi.org/10.1029/2012JF002402

McSaveney, E. R. (1971). *The surfacial texture of rockfall talus*. M.Sc. Thesis. Ohio State University.thesis.

Ng, C. W., Liu, H., Choi, C. E., Kwan, J. S., & Pun, W. K. (2021). Impact dynamics of boulder-enriched debris flow on a rigid barrier. *Journal of Geotechnical and Geoenvironmental Engineering*, *147*(3), 04021004. https://doi.org/10.1061/(asce)gt.1943-5606.0002485

Nie, J., Zhao, S., Cui, Y., & Wang, Y. (2022). Coupled effects of particle overall regularity and sliding friction on the shear behavior of uniformly graded dense sands. *Journal of Rock Mechanics and Geotechnical Engineering*. in press. https://doi.org/10.1016/j.jrmge.2021.10.014

Obanawa, H., & Matsukura, Y. (2006). Mathematical modeling of talus development. *Computers & Geosciences*, *32*(9), 1461–1478. https://doi.org/10.1016/j.cageo.2006.05.004

Pabst, W., & Gregorova, E. (2007). Characterization of particles and particle systems. *ICT Prague*, *122*, 122.

Pei, Z. (2016). *The evolution and catastrophic mechanism of talus slopes in Alpine areas*. Doctoral dissertation. Chengdu University of Technology.

Pérez, F. (1998). Talus fabric, clast morphology, and botanical indicators of slope processes on the Chaos Crags (California Cascades), U.S.A. *Géographie Physique et Quaternaire*, *52*(1), 47–68. https://doi.org/10.7202/004861ar

Pérez, F. L. (1985). Surficial talus movement in an Andean paramo of Venezuela. *Geografiska Annaler - Series A: Physical Geography*, *67*(3–4), 221–237. https://doi.org/10.1080/04353676.1985.11880148

Pérez, F. L. (1989). Talus fabric and particle morphology on Lassen Peak, California. *Geografiska Annaler - Series A: Physical Geography*, *71*(1–2), 43–57. https://doi.org/10.2307/521007

Phillips, J. C., Hogg, A. J., Kerswell, R. R., & Thomas, N. H. (2006). Enhanced mobility of granular mixtures of fine and coarse particles. *Earth and Planetary Science Letters*, *246*(3–4), 466–480. https://doi.org/10.1016/j.epsl.2006.04.007

Robinson, D. A., & Friedman, S. P. (2002). Observations of the effects of particle shape and particle size distribution on avalanching of granular media. *Physica A: Statistical Mechanics and its Applications*, *311*(1–2), 97–110. https://doi.org/10.1016/s0378-4371(02)00815-4

Salciarini, D., Tamagnini, C., & Conversini, P. (2010). Discrete element modeling of debris-avalanche impact on earthfill barriers. *Physics and Chemistry of the Earth, Parts A/B/C*, *35*(3–5), 172–181. https://doi.org/10.1016/j.pce.2009.05.002

Sass, O. (2006). Determination of the internal structure of alpine talus deposits using different geophysical methods (Lechtaler Alps, Austria). *Geomorphology*, *80*(1–2), 45–58. https://doi.org/10.1016/j.geomorph.2005.09.006

Sass, O. (2007). Bedrock detection and talus thickness assessment in the European Alps using geophysical methods. *Journal of Applied Geophysics*, *62*(3), 254–269. https://doi.org/10.1016/j.jappgeo.2006.12.003

Savage, S. B., & Lun, C. K. K. (1988). Particle size segregation in inclined chute flow of dry cohesionless granular solids. *Journal of Fluid Mechanics*, *189*, 311–335. https://doi.org/10.1017/S002211208800103X

Saxton, J., Fralick, P., Panu, U., & Wallance, K. (2008). Density segregation of minerals during high velocity transport over a rough bed: Implications for the formation of placers. *Economic Geology*, *103*(8), 1657–1664. https://doi.org/10.2113/GSECONGEO.103.8.1657

Sheng, L. T., Hsiau, S. S., & Hsu, N. W. (2021). Experimental study of the dynamic behavior and segregation of density-bidisperse granular sliding masses at the laboratory scale. *Landslides*, *18*, 2095–2110. https://doi.org/10.1007/s10346-021-01629-1

Sitharam, T. G., Dinesh, S. V., & Shimizu, N. (2002). Micromechanical modelling of monotonic drained and undrained shear behaviour of granular media using three-dimensional DEM. *International Journal for Numerical and Analytical Methods in Geomechanics*, *26*(12), 1167–1189. https://doi.org/10.1002/nag.240

Statham, I. (1976). A scree slope rockfall model. *Earth Surface Processes*, *1*(1), 43–62. https://doi.org/10.1002/esp.3290010106

Thornes, J. B. (1971). *State, Environment and Attribute in Scree-Slope Studies* (Vol. 3, pp. 49–63). Institute of British Geographers, Special Publication.

Utili, S., & Crosta, G. B. (2011a). Modeling the evolution of natural cliffs subject to weathering: 1. Limit analysis approach. *Journal of Geophysical Research*, *116*(F01016). https://doi.org/10.1029/2009jf001557

Utili, S., & Crosta, G. B. (2011b). Modeling the evolution of natural cliffs subject to weathering: 2. Discrete element approach. *Journal of Geophysical Research*, *116*(F01017). https://doi.org/10.1029/2009jf001559

van der Vaart, K., Thornton, A. R., Johnson, C. G., Weinhart, T., Jing, L., Gajjar, P., et al. (2018). Breaking size-segregation waves and mobility feedback in dense granular avalanches. *Granular Matter*, *20*(3), 46. https://doi.org/10.1007/s10035-018-0818-x

Wadell, H. (1932). Volume, shape, and roundness of rock particles. *The Journal of Geology*, *40*(5), 443–451. https://doi.org/10.1086/623964

Wadell, H. (1935). Volume, shape, and roundness of quartz particles. *The Journal of Geology*, *43*(3), 250–280. https://doi.org/10.1086/624298

Wang, W., & Coop, M. R. (2016). An investigation of breakage behaviour of single sand particles using a high-speed microscope camera. *Géotechnique*, *66*(12), 984–998. https://doi.org/10.1680/jgeot.15

Yang, E., Bui, H. H., Nguyen, G. D., Choi, C. E., Ng, C. W., De Sterck, H., & Bouazza, A. (2021). Numerical investigation of the mechanism of granular flow impact on rigid control structures. *Acta Geotechnica*, *16*(8), 1–23. https://doi.org/10.1007/s11440-021-01162-4

Yang, J., & Dai, B. B. (2011). Is the quasi-steady state a real behaviour? A micromechanical perspective. *Géotechnique*, *61*(2), 175–183. https://doi.org/10.1680/geot.8.p.129

Yang, J., & Luo, X. D. (2015). Exploring the relationship between critical state and particle shape for granular materials. *Journal of the Mechanics and Physics of Solids*, *84*, 196–213. https://doi.org/10.1016/j.jmps.2015.08.001

Yang, J., & Wei, L. M. (2012). Collapse of loose sand with the addition of fines: The role of particle shape. *Géotechnique*, *62*(12), 1111–1125. https://doi.org/10.1680/geot.11.p.062

Yang, Z. X., Yang, J., & Wang, L. Z. (2013). Micro-scale modeling of anisotropy effects on undrained behavior of granular soils. *Granular Matter*, *15*(5), 557–572. https://doi.org/10.1007/s10035-013-0429-5

Zhang, Y. C., Huang, R. Q., Fu, R. H., & Pei, X. J. (2010). Experimental research on dynamic failure mechanism of large-scale talus slope. *Chinese Journal of Rock Mechanics and Engineering*, *29*(1), 65–72.

Zhou, B., Wang, J., & Wang, H. (2018). Three-dimensional sphericity, roundness and fractal dimension of sand particles. *Géotechnique*, *68*(1), 18–30. https://doi.org/10.1680/jgeot.16

Zhou, G. G., & Sun, Q. C. (2013). Three-dimensional numerical study on flow regimes of dry granular flows by DEM. *Powder Technology*, *239*, 115–127. https://doi.org/10.1016/j.powtec.2013.01.057

Zhou, G. G. D., Cui, K. F. E., Jing, L., Zhao, T., Song, D., & Huang, Y. (2020). Particle size segregation in granular mass flows with different ambient fluids. *Journal of Geophysical Research: Solid Earth*, *125*(10), e2020JB019536. https://doi.org/10.1029/2020JB019536

Zhou, G. G. D., & Ng, C. W. (2010). Numerical investigation of reverse segregation in debris flows by DEM. *Granular Matter*, *12*(5), 507–516. https://doi.org/10.1007/s10035-010-0209-4